Published in final edited form as:

Cancer Immunol Res. 2022 January ; 10(1): 40–55. doi:10.1158/2326-6066.CIR-21-0326.

Macrophage-Targeted Therapy Unlocks Antitumoral Cross-talk between IFNγ-Secreting Lymphocytes and IL12-Producing Dendritic Cells

Christina Pfirschke[1], **Rapolas Zilionis**[2,3], **Camilla Engblom**[1], **Marius Messemaker**[1], **Angela E. Zou**[1], **Steffen Rickelt**[4], **Nicolas A. Gort-Freitas**[2], **Yunkang Lin**[1], **Ruben Bill**[1], **Marie Siwicki**[1], **Jeremy Gungabeesoon**[1], **Melissa M. Sprachman**[1], **Angela N. Marquard**[1], **Christopher B. Rodell**[1], **Michael F. Cuccarese**[1], **Jeremy Quintana**[1], **Maaz S. Ahmed**[1], **Rainer H. Kohler**[1], **Virginia Savova**[2,5], **Ralph Weissleder**[1,6], **Allon M. Klein**[2], **Mikael J. Pittet**[1,7,8,9,10,11]

[1]Center for Systems Biology, Massachusetts General Hospital Research Institute and Harvard Medical School, Boston, Massachusetts.

[2]Department of Systems Biology, Harvard Medical School, Boston, Massachusetts.

[3]Institute of Biotechnology, Life Sciences Center, Vilnius University, Vilnius, Lithuania.

Corresponding Authors: Mikael J. Pittet, Department of Pathology and Immunology, University of Geneva, 1005 Lausanne, Switzerland. Phone: 41 79 73 73 295; mikael.Pittet@unige.ch; and Allon M. Klein, Department of Systems Biology, Harvard Medical School, 200 Longwood Avenue, Armenise Building 545B, Boston, MA 02115. allon_klein@hms.harvard.edu.

Authors' Contributions

C. Pfirschke: Initiated the study, performed the analyses and prepared the figures, performed mouse experiments, wrote the article. **R. Zilionis:** Data curation, initiated the study, performed the analyses and prepared the figures, carried out scRNA-seq experiments, performed computational analyses. **C. Engblom:** Initiated the study, performed the analyses and prepared the figures, performed mouse experiments. **M. Messemaker:** Performed computational analyses. **A.E. Zou:** Performed computational analyses. **S. Rickelt:** Performed IHC. **N.A. Gort-Freitas:** Performed computational analyses. **Y. Lin:** Performed mouse experiments. **R. Bill:** Performed mouse experiments. **M. Siwicki:** Performed mouse experiments. **J. Gungabeesoon:** Performed mouse experiments, wrote the article. **M.M. Sprachman:** Synthesized the CSF1R inhibitor BLZ945, verified purity, formulated the drug. **A.N. Marquard:** Verified purity of CSF1R inhibitor BLZ945, formulated the drug. **C.B. Rodell:** Verified purity of CSF1R inhibitor BLZ945, formulated the drug. **M.F. Cuccarese:** Verified purity of CSF1R inhibitor BLZ945, formulated the drug. **J. Quintana:** Verified purity of CSF1R inhibitor BLZ945, formulated the drug. **M.S. Ahmed:** Verified purity of CSF1R inhibitor BLZ945, formulated the drug. **R.H. Kohler:** Performed intravital microscopy. **V. Savova:** Carried out scRNA-seq experiments, performed computational analyses. **R. Weissleder:** Provided input for research design and interpretation, edited the article. **A.M. Klein:** Initiated the study, performed the analyses and prepared the figures, supervised the study, wrote the article. **M.J. Pittet:** Conceptualization, data curation, formal analysis, supervision, funding acquisition, writing–original draft, writing–review and editing, initiated the study, performed the analyses and prepared the figures, supervised the study, wrote the article.

Authors' Disclosures

C. Engblom reports personal fees from 10x Genomics outside the submitted work. A.E. Zou reports grants from National Institute of General Medical Sciences during the conduct of the study. N.A. Gort-Freitas reports grants from NIH during the conduct of the study. R. Bill was supported by a Postdoc.Mobility Fellowship of the Swiss National Science Foundation (SNSF; P400PM_183852), and his spouse is an employee and stockholder of CSL Behring. M.M. Sprachman reports grants from NIH during the conduct of the study. M.F. Cuccarese reports other support from Recursion outside the submitted work. V. Savova is an employee of Sanofi. R. Weissleder reports other support from T2 Biosystems, Lumicell, Accure Health, Moderna, and Tarveda Therapeutics outside the submitted work. M.J. Pittet reports grants from ISREC Foundation, Samana Cay MGH Research Scholar, Swiss Cancer League, and NIH during the conduct of the study, as well as personal fees from Molecular Partners, ImmuneOncia, Tidal, Third Rock Ventures, Recursion, MPM, AstraZeneca, Aileron, Siamab, Elstar, Bristol Myers Squibb, Bicycle, Syndax, Secarna, KSQ, and Forma outside the submitted work. No disclosures were reported by the other authors.

The costs of publication of this article were defrayed in part by the payment of page charges. This article must therefore be hereby marked *advertisement* in accordance with 18 U.S.C. Section 1734 solely to indicate this fact.

Supplementary data for this article are available at Cancer Immunology Research Online (http://cancerimmunolres.aacrjournals.org/).

[4]David H. Koch Institute for Integrative Cancer Research, Massachusetts Institute of Technology, Cambridge, Massachusetts.

[5]Precision Immunology, Immunology and Inflammation Therapeutic Area, Sanofi, Cambridge, Massachusetts.

[6]Department of Radiology, Massachusetts General Hospital, Boston, Massachusetts.

[7]Department of Pathology and Immunology, University of Geneva, Geneva, Switzerland.

[8]Ludwig Institute for Cancer Research, Lausanne Branch, Switzerland.

[9]AGORA Cancer Research Center, Lausanne, Switzerland.

[10]Department of Oncology, Geneva University Hospitals, Geneva, Switzerland.

[11]Center for Translational Research in Onco-Hematology, University of Geneva, Geneva, Switzerland.

Abstract

Macrophages often abound within tumors, express colony-stimulating factor 1 receptor (CSF1R), and are linked to adverse patient survival. Drugs blocking CSF1R signaling have been used to suppress tumor-promoting macrophage responses; however, their mechanisms of action remain incompletely understood. Here, we assessed the lung tumor immune microenvironment in mice treated with BLZ945, a prototypical small-molecule CSF1R inhibitor, using single-cell RNA sequencing and mechanistic validation approaches. We showed that tumor control was not caused by $CSF1R^+$ cell depletion; instead, CSF1R targeting reshaped the $CSF1R^+$ cell landscape, which unlocked cross-talk between antitumoral $CSF1R^-$ cells. These cells included IFNγ-producing natural killer and T cells, and an IL12-producing dendritic cell subset, denoted as DC_3, which were all necessary for CSF1R inhibitor–mediated lung tumor control. These data indicate that CSF1R targeting can activate a cardinal cross-talk between cells that are not macrophages and that are essential to mediate the effects of T cell–targeted immunotherapies and promote antitumor immunity.

Introduction

Macrophages are innate immune cells that can heavily infiltrate the tumor microenvironment (TME) and perform various tumor-promoting functions, including suppression of antitumor immune cells, stimulation of angiogenesis, and promotion of cancer cell proliferation, invasion, and metastasis (1–3). Accordingly, high numbers of tumor-associated macrophages (TAM) correlate with poor prognosis for the vast majority of solid tumors (4–6).

Activated macrophages are typically classified into two types, M1 and M2, based on changes in gene expression that arise in response to defined stimuli *in vitro* (7–9). In cancer, M1-like cells are often thought to carry antitumor functions, whereas M2-like cells may foster tumor outgrowth. However, increasing evidence indicates that TAMs do not follow a simple M1–M2 polarization *in vivo* and that the full spectrum of macrophage plasticity is more complex (10–14). This offers both a challenge and opportunity in exploring their role in tumor progression. Because TAMs are genomically stable and respond quickly to

external stimuli, they are considered a therapeutic target for the treatment of various cancer types (15). Targeting TAMs may present an orthogonal or independent mechanistic route to control tumors compared with existing immunotherapies that target T cells and may be particularly relevant in the context of so-called “cold tumors,” which lack T cells but harbor TAMs in high numbers.

At present, several TAM-targeting agents are being tested clinically. These include antagonists of either the CCL2–CCR2 pathway or CCR5 (3, 16) with the aim to limit macrophage recruitment to tumors; antagonists of ANG1/2 and TIE2 to target TAMs with pro-angiogenic properties (3, 17) CD40 agonists (3, 16) and TLR inhibitors (16) to activate TAMs’ antitumor functions; PI3Kg and PI3Kd inhibitors to inhibit TAMs’ immunosuppressive activities (3); CD47 blocking antibodies to enable TAMs to phagocytose cancer cells (3, 16) and CSF1–CSF1R pathway targeting drugs to limit the production of macrophages as well as their recruitment to, and survival in the tumor stroma (3, 16).

TAM targeting with CSF1R-blocking antibodies or kinase inhibitors is successful in controlling the progression of advanced-stage solid tumors in various animal models (16, 18–22), even more so when combined with other forms of treatments, including immunotherapy (23–25), radiotherapy (26, 27), and chemotherapy (28). In patients, CSF1R targeting is efficacious against tenosynovial giant cell tumors, which express high levels of CSF1 and CSF1R (19, 29). Nonetheless, the molecular mechanisms of drug action remain incompletely understood. For example, whereas CSF1R-targeting drugs were originally designed to reduce the number of TAMs, and indeed do so when used as single treatment agents in a number of animal models (16, 19, 22–24, 26, 28), a seminal study showed that successful response to CSF1R inhibitor (CSF1Ri) treatment in a proneural glioma mouse model can occur without triggering TAM depletion, but instead arise through TAM reeducation (21). These findings call for a more detailed understanding of the effects of TAM targeting *in vivo*.

Here, we studied lung adenocarcinoma because our knowledge of CSF1R treatment against this disease remains scarce. In addition, this disease accounts for more than 1 million deaths worldwide each year, making it the leading cause of cancer mortality (30, 31); is often infiltrated by TAMs (10, 32, 33); and the majority of patients who are diagnosed with this disease do not benefit from standard-of-care treatments and thus need new treatment options. We studied the effects of CSF1Ri treatment in the KP1.9 lung adenocarcinoma mouse model, which is driven by oncogenic *Kras* and *Trp53* mutations and recapitulates key features of the human disease (34, 35). Tumor cells of this cell line do not express CSF1R (36). Lung adenocarcinoma nodules growing in these mice typically show a paucity of T cells (34) but are infiltrated by macrophages, similarly to many human lung adenocarcinomas (10, 33). In accordance with the majority of lung cancer patients, KP1.9 tumor–bearing mice are refractory to common treatment options, including immunotherapy (33, 34). Using this model, we investigated the effects of CSF1Ri treatment by using single-cell RNA sequencing (scRNA-seq) to allow for an unbiased, holistic evaluation of the tumor-infiltrated immune cell compartment accompanied by molecular perturbations and examined the expression of identified target genes in human lung tumors.

Our findings revealed how CSF1Ri treatment reshaped the transcriptional landscape of $CSF1R^+$ cells within lung tumors, and consequently how this change rewired cellular cross-talk within the TME. Consistent with recent studies, we observed that the canonical model for TAM activation ("classic" M1 and "alternative" M2 types) did not simply reflect changes induced by treatment. These results thus reinforce the need to move beyond monitoring defined M1 and M2 phenotypes of macrophages to elucidate mechanisms of immunotherapy. We then specifically investigated a fundamental licensing loop (37), which requires the cytokines IL12 and IFNγ, and also mediates T-cell immunotherapies. In doing so, we documented a role for natural killer (NK) cells, T cells, and a dendritic cell (DC) state, referred here to as DC_3, in promoting antitumor immunity triggered by CSF1Ri treatment.

Materials and Methods

Cell lines

The lung adenocarcinoma cell line KP1.9 was derived from lung tumor nodules of a C57BL/6 *Kras*$^{LSL\text{-}G12D/WT;}$*Trp53*$^{flox/flox}$ (KP) mouse and was kindly provided by Alfred Zippelius (University Hospital Basel, Basel, Switzerland). Cell line authentication was assessed by a PCR-based cell check test (IDEXX BioResearch, case no. 25955–2013). KP1.9 cells were maintained in Iscove's DMEM cell culture medium (Corning, catalog no. 10–016-CV) supplemented with 10% FBS (Atlanta Biologicals, catalog no. S12450) and 1% penicillin/streptomycin (Corning, catalog no. 30–002-CI) and generally passaged twice after thawing before injection into mice. The melanoma cell line D4M.3A was kindly provided by Thorsten Mempel (Massachusetts General Hospital Research Institute, Boston, MA). D4M.3A cells were maintained in DMEM cell culture medium (Corning, catalog no. 10–013-CV) supplemented with 10% FBS and 1% penicillin/streptomycin and passaged twice after thawing before injection into mice. MAP testing was performed by PCR and ELISA-based assays to show that KP1.9 (IDEXX BioResearch, case no. 25955–2013) and D4M.3A cells (VRL, accession no. md14006494) were free of adventitious agents including *Mycoplasma*. Additional *Mycoplasma* testing was regularly performed using PCR.

Mice

All mice used for this study were on a C57BL/6 background and purchased from the Jackson Laboratory. Following mouse strains were used: C57BL/6J wild-type (WT) mice (Stock no. 000664; RRID: IMSR_JAX:000664), IFNγ knockout (KO) mice (Stock no. 002287; RRID:IMSR_JAX:002287), Batf3 KO mice (Stock no. 013755; RRID: IMSR_JAX:013755), IL12p40 KO mice (Stock no. 002693; RRID: IMSR_JAX:002693), and IL12p40-IRES-eYFP mice (Stock no. 006412; RRID:IMSR_JAX:006412). All animals were housed under specific pathogen-free conditions at the Massachusetts General Hospital (MGH; Boston, MA). Animal experiments were approved by the MGH Institutional Animal Care and Use Committee (IACUC) and were performed in accordance with MGH IACUC regulations.

Mouse tumor model

Murine KP1.9 lung tumor cells were injected into 10–16 weeks old female mice intravenously [2.5×10^5 cells in 100 μL PBS (Corning, catalog no. 21–040-CV)] to develop orthotopic tumors in the lung or intradermally to the flank (2×10^6 cells in 50 μL PBS). If not stated otherwise in the respective figure legends, daily drug treatment of lung tumor–bearing mice started 4 weeks after tumor cell injection, when tumor nodules were macroscopically detectable in the lung, and mice were typically euthanized after 2 weeks (14 drug injections). The mice were assigned to the treatment groups at random and the body weight of the mice was measured throughout the experiments. Evaluation of lung tumor burden included lung weight measurements and histologic analyses based on hematoxylin and eosin (H&E) stainings on explanted lung tissue sections to define the tumor area *in situ* as described previously (34). Treatment of flank tumor–bearing KP1.9 C57BL/6J WT female mice started 1 week after tumor cell injection and was performed for 8 consecutive days. Mice were euthanized 1 day after the last drug injection. Murine D4M.3A melanoma cells were injected into 8-week-old male C57BL/6J WT mice intradermally to the flank (1×10^6 cells in 50 μL PBS). Daily drug treatments of tumor-bearing D4M.3A mice started 8 days after tumor cell injection and were performed for 8 consecutive days. Mice were euthanized 1 day after the last drug injection. Tumor dimensions were measured with a digital caliper and tumor volumes defined as $\pi/6 \times \text{length} \times \text{width}^2$. Mouse tumors were allowed to grow to a maximum of 2 cm in diameter, or until tumor ulceration occurred. Age- and sex-matched mice were used as treatment controls and tumor-free, healthy controls. Number of murine replicates is indicated in the figure legend of the respective figure panels that show mouse experimental data.

In vivo CSF1 receptor inhibition

The small-molecule BLZ945 was used as CSF1 receptor inhibitor in this study. The drug was either synthesized in the laboratory of Ralph Weissleder (Center for Systems Biology, MGH, Boston, MA) or provided by Novartis. BLZ945 was formulated in 20% weight per volume (2-hydroxypropyl)-β-cyclodextrin (HPβCD, Trappsol, USP-grade, Cyclo Therapeutics) dissolved in 1 × PBS. To ensure complete dissolution, the formulation was stirred, sonicated, and centrifuged. Final BLZ945 concentration was determined using liquid chromatography-mass spectrometry (LC-MS) by comparison to a standard curve. LC-MS data were obtained using a Waters instrument equipped with a Waters 2424 ELS Detector, Waters 2998 UV-VIS detector, and Waters 3100 mass detector. Analytic separations were carried out using a Waters Xterra C18 5 μmol/L column with eluents (0.1% formic acid, volume per volume) in acetonitrile/water, with a gradient as follows: 0 to 1.5 minutes, 5% to 100%, 1.5 to 2 minutes, 100% acetonitrile. If no precipitate was observed, the solution was sterile filtered (0.22 μm filters) and used for murine injections. In general, mice received 100 mg/kg BLZ945 or vehicle solution (20% HPβCD in 1 × PBS) in 100 to 150 μL depending on sample concentration (ranging from 16.7–25 mg/mL) intraperitoneally once daily. In some experiments with KP1.9 flank tumor–bearing mice, injections were also performed intravenously. If not stated otherwise, BLZ945 or vehicle only (for control mice) were injected for 14 days into KP1.9 lung tumor–bearing mice and for 8 days into mice bearing KP1.9 or D4M3.A flank tumors.

In vivo CD8$^+$ and NK1.1$^+$ cell depletion

To investigate whether cytotoxic T cells and NK cells are relevant for BLZ945 treatment efficacy, these cells were depleted in KP1.9 lung tumor–bearing mice that received BLZ945 or control vehicle injections. BLZ945 treatment started 4 weeks after tumor cell injection and was performed daily for 2 weeks. Mice were euthanized 1 day after the last BLZ945 injection. T-cell and/or NK-cell depletion started 4 days before the first BLZ945 drug injection and was continued every second day for T-cell depletion and every fourth day for NK-cell depletion until the end of the experiment. CD8$^+$ T cells were depleted by performing intraperitoneal injections of CD8a antibodies (clone 53–6.7, BioXcell, 200 μg/mouse, catalog no. BE0004–1; RRID: AB_1107671). For depletion of NK cells, mice received NK1.1 anti-bodies intraperitoneally (clone PK136, BioXcell, 200 μg/mouse, catalog no. BE0036; RRID:AB_1107737). The antibodies were diluted in 1 × PBS. The efficacy of CD8 T-cell and NK-cell depletion was verified by flow cytometry.

Recovery of single-cell suspensions from murine lung

Single-cell suspensions were isolated from murine lungs and kept on ice or at 4°C for all steps if not stated otherwise. Lungs were harvested, cut into small pieces using scissors, and digested in 10 mL RPMI medium (Corning, catalog no. 10–040-CV) containing 0.2 mg/mL collagenase type I (Worthington Biochemical Corporation, catalog no. LS004197) for 1 hour at 37°C while shaking (225 rpm). Digested lung tissue was gently meshed through 40 mm cell strainers (Thermo Fisher Scientific) using a plunger. Red blood cells were removed using 1 mL ammonium-chloride-potassium (ACK) lysis buffer (Lonza, catalog no. 10–548E) for 1 minute at room temperature and the reaction was stopped with RPMI medium. The resulting single-cell suspensions were washed and resuspended in flow cytometry washing buffer (PBS containing 0.5% BSA (VWR, catalog no. 97061–422) until used for flow cytometry staining.

Flow cytometry

Single-cell suspensions from lung tissue were obtained as described above. To verify CD8 T-cell and NK-cell depletion from lung tissues, single cells were washed with 1 × PBS and dead cells stained using the Zombie Aqua fixable viability Kit (BioLegend, catalog no. 423102) while incubating the cells for 20 minutes at room temperature. Afterward, the cells were washed with flow cytometry staining buffer [PBS containing 0.5% BSA and 2 mmol/L ethylenediaminetetraacetic acid (EDTA, Sigma-Aldrich, catalog no. E7889)] and incubated with FcBlock (TruStain FcX, anti-mouse CD16/32, clone 93, BioLegend, catalog no. 101320; RRID:AB_1574975) for 15 minutes followed by staining with fluorescent-conjugated antibodies for 45 minutes at 4°C. After a washing step using flow cytometry staining buffer, cells were fixed with the Fixation/Permeabilization Solution Kit (BD Biosciences, catalog no. 554714) for 20 minutes at 4°C. The cells were washed with 1 × perm wash buffer and analyzed on a LSRII flow cytometer (BD Biosciences) using BD FACSDiva (RRID:SCR_001456) and FlowJo (RRID:SCR_008520) software.

7-aminoactinomycin D (7AAD, Sigma, catalog no. A9400) positivity was used to exclude dead cells from lung tissues stained for monocytes and macrophages. In this case, single cells stained with fluorescent-conjugated antibodies were washed with flow cytometry

staining buffer and incubated with 7AAD directly before analysis at the flow cytometer. Doublet cells were excluded on the basis of their forward/side scatter properties. The number of cells per mg lung tissue was calculated on the basis of the percentage of each cell type identified by flow cytometry multiplied by the total number of cells in each organ. Cell numbers were obtained by determining viable cell numbers based on the trypan blue exclusion method. For this method, single-cell suspensions were mixed with trypan blue solution (VWR, catalog no. 45000–717) and viable cells, which exclude the trypan blue dye, manually counted using a hematocytometer.

On the basis of cell surface marker expression, the following cell states were identified by flow cytometry: monocytes ($CD45^+$ $CD11b^+$ Ly-$6G^-$ Ly-$6C^+$), $CD11b^+$ macrophages ($CD45^+$ $CD11b^+$ Ly-$6G^-$ Ly-$6C^-$ $CD11c^+$ $F4/80^+$), $CD11b^-$ macrophages ($CD45^+$ $CD11b^-$ $CD11c^+$ $F4/80^+$), $CD8a^+$ T cells ($CD45^+$ $CD3^+$ $CD4^-$ $CD8a^+$), $CD8b^+$ T cells ($CD45^+$ $CD3^+$ $CD4^-$ $CD8b^+$), $CD49b^+$ NK-like cells ($CD45^+$ $CD3^-$ $CD49b^+$). NK-cell antibody depletion using NK1.1 antibody (clone PK136, BioXcell, catalog no. BE0036; RRID: AB_1107737) was evaluated by flow cytometry staining containing the marker CD49b because the NK1.1 epitope may be masked by the depleting antibody. CD8 cell antibody depletion using CD8a antibody (clone 53–6.7, BioXcell, catalog no. BE0004–1; RRID:AB_1107671) was evaluated using CD8a and CD8b antibodies.

Following antibodies were purchased from BD Biosciences: CD8a (clone 53–6.7, catalog no. 553031; RRID:AB_394569), CD11b (clone M1/70, catalog no. 557657; RRID:AB_396772), CD4 (clone RM4–5, catalog no. 552775; RRID:AB_394461); and BioLegend: CD45 (clone 30-F11, catalog no. 103126; RRID:AB_493535), CD8b (clone YTS156.7.7, catalog no. 126620; RRID:AB_2563951), CD49b (clone DX5, catalog no. 108910; RRID:AB_313417), CD3 (clone 145–2C11, catalog no. 100308; RRID:AB_312673), F4/80 (clone BM8, catalog no. 123114; RRID:AB_893478), Ly-6G (clone 1A8, catalog no. 127622; RRID:AB_10643269), CD11c (clone N418, catalog no. 117333; RRID: AB_11204262), Ly-6C (clone HK1.4, catalog no. 128037; RRID: AB_2562630).

Flow cytometry–based sorting of $CD45^+$ cells from lung tissues

Single-cell suspensions were obtained from KP1.9 lung tumors of C57BL/6 female mice that were treated for 15 days with BLZ945 or vehicle control solution ($n = 2$ mice per condition). Treatment started on day 29 following intravenous tumor cell injection, and lungs were harvested on day 44 as described before (10). Briefly, mice were perfused with PBS (37°C) and lung tumor tissues macroscopically dissected using surgical fine scissors. Small, equally sized tissue pieces were digested (RPMI medium containing 0.2 mg/mL collagenase type I) for 15 minutes at 37°C while shaking (700 rpm). Digested lung tissue was gently meshed through 70 mm cell strainers using a plunger and single-cell suspensions stained with a fluorescent-conjugated antibody specific to CD45 (clone 30-F11, BioLegend, catalog no. 103126; RRID: AB_493535) for 45 minutes at 4°C. The cells were washed with flow cytometry staining buffer (PBS containing 0.5% BSA and 2 mmol/L EDTA) and $CD45^+$ live cells sorted on a FACS Aria cell sorter (BD Biosciences) into FBS-containing reaction tubes, which were kept on ice until the cells were further processed for scRNA-seq.

7AAD was used to exclude dead cells during sorting. In this study, previously generated scRNA-seq data from healthy tumor-free lung tissue of C57BL/6 male mice (10) [Gene Expression Omnibus (GEO): GSE127465, $n = 2$] were used in parallel. Lung cells from tumor-free mice for single-cell encapsulation were obtained following the same protocol as described above.

Histology

For histologic analysis of lung tumor burden to define the percent tumor tissue area per lung lobe section, murine lung lobes were harvested, formaldehyde fixed, and paraffin embedded as described before (34), following standard procedures. Consecutive sections were prepared and stained with H&E using the Shandon Varistain Gemini ES Automated Slide Stainer (Thermo Fisher Scientific).

IHC was performed on lung tissue sections as described previously (34) using an automated staining system (LabVision Autostainer 360, Thermo Fisher Scientific). Briefly, individual sections were dewaxed, rehydrated, and treated with heat-induced epitoperetrieval prior to immunostaining using a decloaking chamber (Biocare Medical). The sections were incubated in 10 mmol/L sodiumcitrate (pH6.0, Sigma-Aldrich, catalog no. S1804) buffered solutions containing 0.05% Tween (Sigma-Aldrich, catalog no. P9416) at 120°C for 2 minutes. After blocking endogenous peroxidase and alkaline phosphatase activity (BLOXALL, Vector Laboratories, catalog no. SP6000) and blocking with normal goat (Vector Laboratories, catalog no. S-1000) or horse (Vector Laboratories, catalog no. S-2000) serum (both for 10 minutes) sections were incubated with primary antibodies for 1 hour followed by several washes in PBS and by secondary ImmPRESS polymer detection systems (Vector Laboratories, catalog no. MP-7444, catalog no. MP-5401, catalog no. MP-5402) according to the manufacturer's protocol. Subsequently, the Vulcan Fast Red Chromogen Kit 2 (red staining, Biocare Medical, catalog no. 50–828-59) or DAB Quanto Detection System (brown staining, Thermo Fisher Scientific, catalog no. TA-060-QHDX) were applied as substrates and hematoxylin used as counterstain. Image documentation was done using the NanoZoomer 2.0-RS slide scanner system (Hamamatsu) with NanoZoomer Digital Pathology software or the Leica Aperio AT2 slide scanner system (Leica Biosystems) using Aperio ImageScope software (RRID:SCR_020993). Following primary anti-bodies were used in this study: rat anti-CD8a (clone 4SM15, eBioscience, catalog no. 14–0808-80; RRID:AB_2572860), mouse anti-NK1.1 (clone PK136, Thermo Fisher Scientific, catalog no. MA1–70100; RRID:AB_2296673), rabbit monoclonal anti-F4/80 (clone D2S9R, Cell Signaling Technology, catalog no. 70076; RRID: AB_2799771), and anti-CD3 (clone SP7, Abcam, catalog no. 16669; RRID:AB_443425).

H&E-stained slides were used to identify the tumor area on murine lung sections. On consecutive sections, CD3 positivity was measured using Fiji software (RRID:SCR_002285). In detail, tumor nodules positive for CD3 and nodules lacking CD3 staining were defined using the NanoZoomer Digital Pathology software. Images were taken at 5×, individual tumor areas circled and analyzed using Fiji. The color deconvolution plugin was used to extract the CD3 signal (Fast Red). Thresholded images were quantified

using the Analyze Particles tool and the percent CD3 area per individual tumor nodule was calculated based on the total area pixel and the cell count pixel values.

Intravital microscopy

IL12p40-eYFP reporter mice bearing KP1.9 lung tumors were treated intraperitoneally with the BLZ945 drug or vehicle (start day 29) for 14 consecutive days. Mice were euthanized 43 days after tumor cell injection and lungs immediately imaged *ex vivo*. Cascade Blue Dextran (10 mg/mL, 10KD, Thermo Fisher Scientific, catalog no. D1976) was injected retroorbitally (50 μL) 1 day prior to sacrifice for labeling of phagocytic cells including macrophages. For vasculature staining, 50 μL Griffonia (Bandeiraea) Simplicifolia Lectin I, Rhodamine (2 mg/mL, Vector Laboratories, catalog no. RL-1102–2) was injected retroorbitally 10 minutes before euthanasia. Mice were euthanized and lungs carefully removed, stored in PBS on ice protected from light and immediately imaged for dextran, rhodamine, and endogenous eYFP signals using an Olympus FluoView FV1000MPE confocal imaging system (Olympus America). A 2×air objective XL Fluor 2×/340 (NA 0.14, Olympus America) was used to select tumor areas before switching to a higher magnification for better resolution. Higher magnification Z stack images were obtained using either a XLUMPLFL 20× or 10× water immersion objective (NA 1.0, Olympus America). Sequential scanning (4 or 5 μm step size) with 405, 473, and 559 nm lasers with a DM405/473/559 nm dichroic beam splitter was performed. Beam splitters (SDM473, SDM560) and emission filters (BA430–455, BA490–540, BA575–675) were sourced from Olympus America. Images were Z-projected using Fiji software. Cascade Blue Dextran (macrophages) and eYFP (IL12)-positive cells were manually quantified per field of view in a blinded manner.

Single-cell RNA barcoding, sequencing, and read processing

InDrops scRNA-seq was performed as described before (10, 38, 39) with changes to DNA primers listed in Supplementary Table S1. Single-cell transcriptome barcoding was performed by co-encapsulating cells, barcoding reverse transcription (RT) primers attached to polyacrylamide beads, and RT (SuperScript III, Thermo Fisher Scientific, catalog no. 18080–044) and lysis (Igepal CA-630, Sigma-Aldrich, catalog no. 5674) reagents into 2–3 nL droplets, followed by primer release and RT at 50°C. The resulting barcoded cDNA was taken through the following sequencing library preparation steps: (i) second strand synthesis (NEBNext mRNA Second Strand Synthesis Module, NEB, catalog no. E6111S); (ii) linear amplification by *in vitro* transcription (HiScribe T7 High Yield RNA Synthesis Kit, NEB, catalog no. E2040S); (iii) fragmentation (RNA Fragmentation Reagents, Ambion/Life Technologies, catalog no. AM8740); (iv) RT (PrimeScript Reverse Transcriptase, Takara Clontec, catalog no. 2680A) using random hexamer primers bearing a universal PCR primer annealing site; and (v) indexing PCR (Kapa 2× HiFi HotStart PCR mix, Kapa Biosystems, catalog no. KK2601). The NextSeq Illumina platform was used for sequencing [NextSeq 500/550 High Output Kit v2.5 (75 Cycles), Illumina, catalog no. 20024906]. Read lengths are summarized in Supplementary Table S1. Barcoding in drops was performed on a custom-built microfluidic setup, using barcoding hydrogel beads produced in the Klein lab (Department of Systems Biology, Harvard Medical School, Boston, MA). A detailed description of the inDrops methods, including all reagents and suppliers used in the current study, is available in our Nature Protocols publication (38).

All reads, including those for the tumor-free condition, which were published previously (10), were processed with the inDrops.py pipeline (https://github.com/indrops/indrops) using the same parameters available at https://github.com/AllonKleinLab/paper-data/tree/master/Pfirschke_et_al_2021. Briefly, the inDrops.py pipeline first filtered reads for the presence of (i) cell barcode sequence, (ii) unique molecular identifier, (iii) Illumina library index. Read 1 was then trimmed using Trimmomatic (version 0.32; parameters: LEADING:28 SLIDINGWINDOW:4:20 MINLEN:30), and barcodes were matched against a known whitelist. Reads were split by barcode into separate fastq files. Alignment to the mouse transcriptome was performed using Bowtie (version 1.1.1, parameters: -n 1 -l 12 -e 70 -m 200 -best -strata-a). The reference transcriptome was built using annotations from ENSEMBL (genome assembly GRCm38). inDrops.py performed the UMI correction and returned a gene expression count matrix.

scRNA-seq data filtering, visualization, doublet removal, and annotation

Analyses detailing scRNA-seq data are provided at https://github.com/AllonKleinLab/paper-data/tree/master/Pfirschke_et_al_2021. Cells with <1,000 counts or >15% counts from mitochondrial genes were filtered out. Data was visualized in two-dimensional presentation using SPRING (40), which outputs an interactive force-directed layout of a k-nearest neighbor graph of cells (https://kleintools.hms.harvard.edu/tools/springViewer_1_6_dev.html?data-sets/pittet/mouse/CSF1Ri/all_Cd45pos_cells).

Doublet scores for each cell were calculated using Scrublet (41), and doublet-enriched spectral clusters were removed. Each cell was classified by one of previously published (10) immune cell expression profiles using a Bayesian classifier modeling multinomial count statistics as described before (10, 42, 43). For final cell population annotations used throughout this publication, spectral clusters were labeled after their dominant Bayesian classifier result obtained at the single-cell level, and ambiguous classification cases were annotated manually. Within the murine T_Cd8_IFNγ T-cell state, we observed a cell subset that expresses gamma-delta T-cell receptor genes (*Tcrg-C2*, *Tcrg-C1*) and no *IFNg*. These putative gamma-delta effector T cells have a very similar transcriptome to IFNγ-expressing $CD8^+$ T cells. Unsupervised spectral clustering failed to resolve these cells from IFNγ-expressing $CD8^+$ T cells, even after increasing resolution of spectral clustering. In this study, we therefore have not separated putative gamma-delta T cells from IFNγ-expressing $CD8^+$ T cells.

Unless specified otherwise, all further analyses used normalized counts (counts per 10,000, or CP10K), where the gene expression of each cell was scaled to sum to 10,000 counts. When calculating fold changes in gene expression, a pseudovalue of 1 CP10K was added to prevent infinite fold-change values due to division by zero.

Gene set enrichment analysis

We used a fast gene set enrichment analysis (GSEA) method (fgsea; ref. 44) to identify biological pathways that were significantly over-represented among genes upregulated by CSF1Ri treatment in monocytes and macrophages. To compile a comprehensive set of pathways, we obtained all 12,347 Gene Ontology Biological Process terms and their

associated mouse genes from GO (45) on 23 Nov 2019. We then ranked the genes that were significantly differentially expressed (FDR < 0.05, $|\log_2 FC|>1$) in CSF1Ri-treated monocytes and macrophages by signed fold change in descending order. We ran fgsea on the ranked genes and pathways with permutation number set to 10,000 and excluded pathways in which <15 genes or >300 genes mapped to the ranked gene lists. For specific pathways significantly enriched with CSF1Ri treatment (normalized enrichment score > 0, $P_{\text{adjusted}} < 0.05$), we calculated a score for the pathway within each monocyte/macrophage state by taking the sum of the average expression (in CP10K) of each "leading-edge" gene in the pathway. The leading-edge genes are defined as the core set of genes that contribute to the enrichment signal calculated by GSEA (46).

Ligand–receptor analysis

We defined a list of 2,017 mouse ligand-receptor pairs based on an existing human ligand-receptor dataset (47) and manually curated interactions from InnateDB (48). We then applied the CellPhoneDB statistical framework (49) to these ligand–receptor pairs and the scRNA-seq data to identify putative ligand–receptor interactions occurring between different cell states. CellPhoneDB was run with permutation number set to 1,000 and with exclusion of interactions in which <5% of cells belonging to the interacting cell types expressed the ligand or receptor. An interaction $l_A r_B$ involving ligand l on cell type A and receptor r on cell type B was defined as enriched with CSF1Ri treatment if it exhibited both significant likelihood of cell-type specificity in CSF1Ri ($P < 0.05$ for $l_A r_B$ and $P < 0.05$ in no more than 10% of all $l_X r_Y$ assessed) and higher ligand–receptor expression in CSF1Ri than in vehicle. Ligand–receptor expression, $\exp(l_A r_B)$, was set as 0 if either mean(gene l in cell type A) and mean(gene r in cell type B) were equal to zero; otherwise, it was defined as the sum of both means. Similarly, an interaction $l_A r_B$ was hypothesized to be diminished with CSF1Ri treatment if it exhibited both significant likelihood of cell-type specificity in vehicle and greater ligand–receptor expression in vehicle than CSF1Ri. All interactions with low expression ($\exp(l_A r_B) < 1$) or minimal relative change between vehicle and CSF1Ri ($|\log_2 FC|< 0.2$) were excluded. Finally, we manually annotated the functional significance of all remaining interactions in terms of their putative or unknown roles in immune activation and suppression. Relative expression of ligands and receptors corresponding to putative interactions was independently computed for each cell type from vehicle-treated samples of KP1.9 tumor–bearing mice and each analogous cell type from an immune dataset derived from human patients with non–small cell lung cancer (NSCLC; ref. 10; GEO: GSE127465). The relative expression values obtained from murine and human datasets for each cell type were contrasted in scatterplots. We computed the Pearson correlation between relative expression values across species to test whether these interactions are present in human tumor-associated immune populations.

Differential gene expression analysis

A gene J was enriched in a cell state c_i if:

Gene J was expressed in at least five cells with at least five CP10K across all cells C.

Gene J was significantly higher expressed in cell state c_i compared with the complement set (all cells in C not in c_i), a two-tailed Mann–Whitney U test with multiple hypothesis correction was used, FDR < 5%.

Data and code availability

scRNA-seq data generated in this study are available at the NCBI GEO depository under the accession number: GSE161771. The data include count-matrices pre- and post-normalization, per-cell meta, and raw FASTQ files. Code for selected analyses to generate figure panels is available at https://github.com/AllonKleinLab/paper-data/tree/master/Pfirschke_et_al_2021.

Statistical analysis of flow cytometry, histology, intravital microscopy, or tumor burden data

All statistical analyses were performed using GraphPad Prism software (RRID:SCR_002798). Results were expressed as mean ± SEM or mean SD as indicated in each respective figure legend. Student two-tailed t test or Student one-tailed t test were done to compare two groups. P values > 0.05 were considered not significant (n.s.); P values < 0.05 were considered significant. *, $P < 0.05$; **, $P < 0.01$; ***, $P < 0.001$; ****, $P < 0.0001$.

Results

CSF1Ri treatment controls KP1.9 lung adenocarcinoma progression

Considering that the CSF1/CSF1R axis promotes the functions and survival of TAMs (23), we examined whether targeting CSF1R pharmacologically affected the growth of established lung adenocarcinomas. Specifically, KP1.9 lung tumors, which were highly infiltrated by F4/80$^+$ cells (Fig. 1A), were allowed to grow orthotopically in mice for 4 weeks, before receiving intraperitoneal treatment with the CSF1Ri BLZ945 dissolved in (2-hydroxypropyl)-β-cyclodextrin (or vehicle alone), daily for 14 days (Supplementary Fig. S1A). Using lung weight as a proxy for tumor burden (50), we observed increased tumor burden on day 43 in both vehicle-treated mice and in untreated control mice (Fig. 1B). In contrast, the lung weight of CSF1Ri-treated mice at day 43 was significantly lower than that of vehicle-treated mice and comparable with lung weights measured on day 27, before initiation of CSF1Ri treatment (Fig. 1B).

We also used H&E-based histology of lung sections to assess tumor burden and revealed a substantial decrease in tumor cross-sectional area following CSF1Ri treatment (Fig. 1C and D). These findings also indicate that H&E-based tumor area quantifications and lung weight measurements reflect each other (34). For subsequent lung tumor burden evaluations in this study, we measured lung weights. We further extended our analyses to KP1.9 tumors grown intradermally in the flank (Supplementary Fig. S1B) and also compared intravenous and intraperitoneal administration of CSF1Ri. We found that CSF1Ri treatment controlled tumor growth, independent of anatomical location and route of drug delivery (Supplementary Fig. S1C and S1D). Taken together, these data indicate that CSF1R inhibition can profoundly restrain the progression of established KP1.9 tumors grown orthotopically in the lung or in

the flank. To extend our analyses to another orthotopic cancer model, we evaluated mice bearing D4M.3A melanoma tumors in the flank (Supplementary Fig. S1E). With this model, we also observed a reduction in tumor growth in 50% of the treated mice (Supplementary Fig. S1F). Using an artificial cutoff of 150 mm^3 at day 16 tumor burden, we found that 4 of 8 (50%) of CSF1Ri-treated mice were below the cutoff in contrast to only 1 of 8 (12.5%) vehicle-treated mice. It is likely that the composition of the tumor immune microenvironment in different tumor models affects the efficacy of macrophage-targeting agents such as BLZ945. To better understand the functionality of the drug, we next focused on KP1.9 lung tumors, as this model showed the strongest response to CSF1Ri treatment.

CSF1Ri treatment reshapes the CSF1R$^+$ cell landscape in NSCLC

The primary motivation to design CSF1R-blocking drugs has been to ablate or reduce the number of macrophages (16, 19, 22, 23, 26, 28); however, CSF1R targeting can also control tumor growth through additional mechanisms (21). Because KP1.9 lung tumors contain monocytes and macrophages in various phenotypic states (10), we sought to fully characterize them in mice that received either CSF1Ri treatment or vehicle only. To this end, we purified CD45$^+$ cells obtained from the lungs of mice that received the different treatment strategies and analyzed cell-type composition by scRNA-seq (2 mice per condition, 25,039 cells post-filter; Fig. 2A; Supplementary Fig. S2A; Supplementary Table S1). To identify changes to steady-state condition, we included previously obtained scRNA-seq data of healthy lung tissue in our analyses (10). We identified the cell types in these data by classifying single-cell transcriptomes to states annotated previously in this lung tumor model (ref. 10; Fig. 2B).

An unsupervised visualization of the scRNA-seq data using SPRING plots (40) revealed the immune populations previously reported in lung adenocarcinoma (10), including monocyte states [classical ($Mono_1$) and non-classical ($Mono_2$); neutrophilic-like ($Mono_3$)]; and MonoDC; and a spectrum of differentiated macrophage states ($Mø_{1,2,3,4}$), including distinct tissue-resident alveolar macrophages ($Mø_4$; Fig. 2C). With the exception of one cluster, these monocyte and macrophage states showed unique gene signatures that reproduced those seen previously in lung tissue (Fig. 2D; Supplementary Fig. S2B; Supplementary Table S2; ref. 10). The exception was cluster $Mø_1$, which failed to reproduce the unique marker genes classified previously, but nonetheless was a reproducible state across replicates, with distinct gene expression from other macrophage clusters (Supplementary Fig. S2C; Supplementary Table S2). *Csf1r* was most highly expressed by monocytes and macrophages in the analyzed lung samples (Supplementary Fig. S2D; Supplementary Table S3) and was expressed by each individual Mono/Mø state (Supplementary Fig. S2E). Expression of *Csf1r* in these myeloid cell states was 4.4-fold above average expression level of other CD45$^+$ cells.

CSF1Ri treatment did not deplete monocytes/macrophages from the lung-resident CD45$^+$ population, as measured by scRNA-seq (Fig. 2E). The difference was significant (Fisher exact test) but the size of the effect between the CSF1Ri- and vehicle-treatment conditions (1.28-fold) was comparable to that between the two replicates of the vehicle group (1.31-fold). Independent analysis by flow cytometry also indicated that CSF1Ri treatment did not decrease monocyte/ macrophage cell counts in KP1.9 tumor–bearing lungs, but rather, the

proportion of these cells increased following CSF1Ri treatment (Supplementary Fig. S2F and S2G). The different strategies to identify monocytes/macrophages (gating an antigen profile common to monocytes and macrophages, as opposed to transcriptome classification) may be responsible for the discrepancy. Our scRNA-seq data revealed significant changes in the abundance of individual monocyte/macrophage populations (Fisher exact test, FDR <1%). We observed a reduction in the differentiated $M\phi_1$ and $M\phi_3$ macrophage states, and an increase in undifferentiated monocytes ($Mono_2$ and $Mono_3$), MonoDC and $M\phi_4$ (Fig. 2F; Supplementary Fig. S2H). CSF1Ri-induced gene expression changes in each monocyte and macrophage state are shown in Supplementary Fig. S3A and S3B.

CSF1Ri treatment reduces CSF1R$^+$ cells' tumor-promoting phenotypes

To investigate how changes in *Csf1r*$^+$ cell states might restrain tumor growth in CSF1Ri-treated mice, we analyzed the monocyte and macrophage transcriptomes to identify putative pro-tumor or antitumor cellular phenotypes and their change upon treatment. We compared the transcriptome of each cell state with canonical M1 and M2 macrophage signatures that have been previously associated with pro- and anti-inflammatory phenotypes (10, 51).

The monocyte and macrophage states did not present an M1-like gene expression profile without CSF1Ri treatment; with treatment, we observed a slight induction of some M1-associated genes in some states, but generally the M1 signature was lacking (Fig. 2G). Several states expressed M2-associated genes in absence of treatment. For example, $M\phi_3$ expressed *Cd163*, *Arg1*, and *Msr1* (also referred to as *Cd204*), which have all been associated with immunosuppression (52–54); however, the paucity of this state was apparent already before treatment and even more so after (Fig. 2F). Also, $Mono_1$, $Mono_3$, and $M\phi_4$ expressed the M2-associated gene *Chil3* in vehicle-treated mice, whereas expression of this gene decreased in the same states in mice treated with CSF1Ri (Fig. 2G). Each of these three states represented approximately 1% of CD45$^+$ cells before treatment, and between 1% and 3% after treatment (i.e., their prevalence was maintained or further increased; Fig. 2F), but they did not express other M2-associated genes following CSF1Ri treatment with the exception of *Chil4* and *Mrc1* that were expressed by $M\phi_4$ (Fig. 2G). These data indicate that tumor control triggered by CSF1Ri treatment was not associated with the emergence of M1-like monocyte and/or macrophage states in the TME. Tumor control may be associated with a decrease of some M2-like phenotypes, but these changes are modest.

To gain a clearer view of how macrophage states mediate an antitumor response following treatment, we took a complementary approach to study changes in gene expression by looking for gene sets that were statistically enriched in expression after treatment (Fig. 2H; Supplementary Table S4). Following treatment, monocytes and macrophages increased expression of genes that showed a strong statistical enrichment for sets associated with antigen processing and presentation, cytokine induction and lymphocyte activation—processes that are important for tumor control. The observed gene expression changes were not confined to a single monocyte or macrophage state, but rather observed across several *Csf1r*$^+$ cell states (Fig. 2I). These data suggest that CSF1Ri treatment triggered changes in the monocyte and macrophage transcriptional landscape, which ultimately promoted cancer control through activation of CSF1R$^-$ cells and most likely involved lymphocytes.

CSF1Ri treatment rewires cellular cross-talk in the TME

We next explored how other immune cell types in the TME respond to treatment. We examined genes underlying Th1 polarization, related chemokines, and genes associated with the activation of cytotoxic mechanisms frequently involved with tissue-specific destruction (55). We found that these genes indeed increased in expression following CSF1Ri treatment (Fig. 3A; Supplementary Fig. S4A). They were not directly expressed by $CSF1R^+$ cells (monocytes/macrophages) but instead by other cell types, including NK cells, T cells, and DCs. These observations complement the GSEA on monocytes and macrophages (Fig. 2H and I) to suggest that CSF1Ri treatment stimulated inflammatory cell–cell interactions within the TME to promote cancer control.

To predict which specific cell state interactions might change in response to CSF1Ri treatment, we searched the scRNA-seq data for cognate ligand–receptor pairs that vary in gene expression between conditions. We used a dataset of human ligand–receptor pairs (47) to develop a list of mouse orthologs comprising 2,017 pairs of ligands and receptors (Supplementary Table S5). We then applied CellPhoneDB, a computational pipeline that scores ligand–receptor pairs across single-cell transcriptome clusters (49) and looked for statistically significant changes in these scores between treatment conditions. Finally, we manually annotated the interactions as putatively immune-activating, immune-inhibitory, or unknown interactions based on the nature of either the ligand's or receptor's reported role in literature (Supplementary Table S6). Our results highlight interactions between immune cell states that either increased, decreased, or remained unchanged (Fig. 3B; Supplementary Fig. S4B). In vehicle-treated mice, we observed multiple ligand–receptor pairs connecting $CSF1R^+$ cells (monocytes/macrophages) with $CSF1R^-$ cells (DCs, NK cells, or T cells). The outcome of many of these interactions was unknown, but several of them were putatively immune-inhibitory (Fig. 3B, left). We did not find significant immune-activating or immune-inhibitory interactions between DCs and NK/T cells, or between T and NK cells in vehicle-treated mice.

In contrast, following treatment, $CSF1R^+$ monocytes/macrophages reduced their signaling interaction with DCs and increased overall interactions with NK cells and T cells (Fig. 3B, right). Again, the outcome of many of the observed interactions between monocytes/macrophages and DC/NK/T cells was unknown; however, we identified a clear increase of putative immune-activating interactions following CSF1Ri treatment between these cells (Fig. 3B, right). The ligand–receptor pairs expressed by monocytes/macrophages and NK/T cells include *Cd80*:*Cd28*, *Cd86*:*Cd28*, *IFNγr1*:*IFNγ*, and *IFNγr2*:*IFNγ* (Fig. 3C; Supplementary Fig. S4C), which are required for lymphocyte stimulation. In the CSF1Ri-treated mice, we observed multiple activating interactions between $CSF1R^-$ cells, that is, between DCs and NK cells, DCs and T cells, and NK cells and T cells (Fig. 3B, right). For example, selected ligand–receptor pairs that appeared following CSF1Ri treatment include *Cd80*:*Cd28*, *Cd86*:*Cd28*, and *Xcr1*:*Xcl1* between DCs and NK/T cells, and *IFNγr2*:*IFNγ*, and *Il12rb2*:*Il12b* between DCs and NK cells (Fig. 3C), among others (Supplementary Fig. S4C). These findings indicated a rewiring of cellular cross-talk in the TME that was triggered by CSF1Ri treatment, extended beyond $CSF1R^+$ to $CSF1R^-$ cells, and may promoted the observed antitumor immune response.

We made use of scRNA-seq data previously collected from patients with NSCLC (10) to compare expression levels of ligands and receptors identified in this study to those in human NK cells, T cells, DCs, and monocytes/macrophages (Supplementary Fig. S4D). The transcript abundances for these genes in each cell type were closely correlated between vehicle-treated KP1.9 lung cancer-bearing mice and human cells from untreated patients with NSCLC (Fig. 3D), suggesting that the baseline signaling landscape modulated by CSF1Ri in mice recapitulated that of the human disease.

Both T cells and NK cells promote CSF1Ri-driven antitumor immunity

We investigated further the role of increased interactions between DCs and NK/T cells in CSF1Ri-driven antitumor responses. Inspection of KP1.9 lung tumor areas by histology revealed a paucity of tumor-infiltrating $CD3^+$ cells in vehicle-treated mice; however, we observed an increase in the percentage of these cells in response to CSF1Ri treatment (Fig. 4A; Supplementary Fig. S5A). Both the quantification of tumor areas that were infiltrated or not by $CD3^+$ cells (Fig. 4B), and of the average $CD3^+$ cell content in individual tumor areas (Supplementary Fig. S5B), confirmed that CSF1Ri treatment promoted tumor infiltration by $CD3^+$ lymphocytes. Repeating this histologic analysis to detect $CD8^+$ cells further showed the enrichment of these cells within KP1.9 lung tumors following CSF1Ri treatment (Fig. 4C). In contrast to T cells, NK cells were already present within tumors from vehicle-treated mice, although only in low numbers (Supplementary Fig. S5C). We further interrogated the relevance of $CD8^+$ T cells by depleting them before and during the CSF1Ri treatment period using an antibody-mediated approach (Supplementary Fig. S5D and S5E). Tumor control triggered by CSF1Ri treatment was lost in mice in which $CD8^+$ T cells were depleted (Fig. 4D, red bar), suggesting that $CD8^+$ T cells were required for CSF1Ri-driven antitumor immunity.

Given that successful responses to anti–PD-1 therapy can rely on IFNγ production (37, 56), we further assessed *IFNγ* expression by scRNA-seq in the KP1.9 lung cancer model (Fig. 4E). We distinguished various lymphocyte states, namely regulatory T cells (Treg), innate lymphoid cells (ILC), gamma delta T cells (γδ T cells), NK cells, $CD4^+$ T cells, as well as two $CD8^+$ T cell states identified on the basis of expression of either *Cxcr3* or *Ccr7* (Fig. 4E and F; Supplementary Fig. S5F and S5G). The $Ccr7^{hi}$ $Cxcr3^{low}$ $CD8^+$ T cells were also $Tcf7^+$ and resembled naïve/memory-like T cells, whereas the $IFNγ^+$ $Cxcr3^{hi}$ $Ccr7^{low}$ $CD8^+$ T cells were also $Gzmk^+$, $Cxcr6^+$, $Lag3^+$, and $Socs2^+$ (Fig. 4F; Supplementary Fig. S5G), and resembled so-called effector/dysfunctional-like $CD8^+$ T cells (57, 58). We found that CSF1R inhibition did not induce the upregulation of *IFNγ* in $CD8^+$ T cells, though the percentage of $Cxcr3^{hi}$ ($Gzmk^+$ $Cxcr6^+$ $Lag3^+$ $Socs2^+$) $CD8^+$ T cells increased after CSF1Ri treatment (Fig. 4G). Nevertheless, IFNγ production by these cells may have biological consequences at the tumor site. In addition, $CD8^+$ T cells may contribute to CSF1Ri-mediated antitumor immunity through mechanisms other than the production of IFNγ.

Besides T cells, we found that CSF1R inhibition induced the upregulation of *IFNγ* by NK cells (Fig. 4E–G; Supplementary Fig. S5H). Consequently, we interrogated the relevance of NK cells by depleting them before and during the CSF1Ri treatment window using

NK1.1 depleting antibodies (Supplementary Fig. S5D and S5E). Tumor control triggered by CSF1R inhibition was lost in mice in which NK cells were depleted (Fig. 4D, yellow bar), suggesting that these cells were required for CSF1Ri-driven antitumor immunity. Following CSF1Ri treatment, NK cells upregulated genes relevant for effector cell functions such as *Tbx21* and *Prf1* (Supplementary Fig. S5I–S5K). These genes can drive antitumor responses: the transcription factor T-bet (encoded by the gene *Tbx21*) controls the expression of IFNγ (59), and perforin 1 (encoded by the gene *Prf1)* is a pore-forming cytolytic protein that destabilizes plasma membranes of target cells and contributes to their lysis (60).

To further assess whether NK-cell and $CD8^+$ T-cell contributions to tumor control are separate or interdependent, we compared tumor burden in mice in which NK cells and $CD8^+$ T cells were depleted simultaneously (Supplementary Fig. S5D and S5E). Combined depletion of NK cells and $CD8^+$ T cells did not further increase tumor burden in the context of CSF1Ri treatment (Fig. 4D, pink bar), suggesting that the actions of both cell types were interdependent. In addition, CSF1Ri-mediated tumor control was lost in *IFNg*-deficient mice (Fig. 4H). This confirms that IFNγ production, which was preferentially produced by NK cells and a subset of $CD8^+$ T cells, was a key event in successful responses to CSF1Ri.

CSF1Ri-driven antitumor immunity requires IL12-expressing DCs

Considering that: (i) IFNγ produced by lymphocytes can stimulate DCs to produce the antitumor cytokine IL12 (37), (ii) CSF1Ri treatment promoted DC interactions with T and NK cells (Fig. 3B, right), some of which expressed IFNγ (Fig. 4E–G; Supplementary Fig. S5H), and (iii) CSF1Ri treatment increased *Il12b* expression by DCs (Fig. 3A and C; Supplementary Fig. S4A), we further examined IL12 activity. Because macrophages may also produce IL12 (61), and are targeted directly by CSF1R inhibition, we sought initially to verify the cellular source of IL12 within KP1.9 lung tumor lesions on protein level and independently of scRNA-seq analysis.

To this end, we used IL12p40-internal ribosome entry site-enhanced yellow fluorescent protein (IL12p40-IRES-eYFP) reporter mice. With these mice, intravital microscopy detects YFP signals from cells that have turned on IL12p40 production (37). We imaged IL12p40-$eYFP^+$ cells in lung tumor tissue of mice treated with CSF1Ri or control vehicle. To identify whether these IL12-producing cells included macrophages, we labeled the latter with Cascade Blue Dextran (62). We also used Lectin Rhodamine to visualize the vasculature and provide spatial context. We found that KP1.9 lung tumor nodules from CSF1Ri-treated mice were infiltrated with macrophages (blue) and IL12-producing cells (green); however, no overlap between YFP and Cascade Blue Dextran signals could be detected, neither in CSF1Ri nor in vehicle-treated mice (Fig. 5A; Supplementary Fig. S6A and S6B), indicating that IL12p40-$eYFP^+$ cells were distinct from macrophages within tumor lesions. These results are consistent with scRNA-seq data, which showed *Il12b* to be expressed at 0.17 counts per ten thousand (CP10K) before treatment and 1.52 CP10K after treatment in DCs but only 0.01 CP10K before treatment and 0.07 CP10K after treatment in monocytes/macrophages.

To further define the source of *Il12b*, we considered that KP1.9 tumors contain three distinct classical DC states (namely, DC_1, DC_2, and DC_3), which are all defined transcriptionally

(10). DC_1 resemble *Xcr1*$^+$ *Clec9a*$^+$ cDC1s, which specialize in antigen cross-presentation and CD8$^+$ T-cell activation; DC_2 resemble *Sirpa*$^+$ cDC2s, which can activate different types of T cells; intratumoral DC_3 lack key cDC1 and cDC2 markers, promote the survival of tumor-infiltrating T cells (63), are necessary for successful immunotherapy in mice (37), are conserved across patients and mice (10, 64, 65), and are also referred to as mregDCs and LAMP3$^+$ DCs (65).

Upon examining the scRNA-seq data for putative ligand–receptor pairs between NK/T cells and each DC state, we detected few ligand: receptor interactions enriched in vehicle-treated mice (Fig. 5B, left; Supplementary Table S6). In contrast, a high number of new ligand–receptor interactions emerged between NK/T cells and all three DC states following CSF1Ri treatment, most of which were putatively immune activating (Fig. 5B, right; Supplementary Table S6). Ligand–receptor pairs that appeared following CSF1Ri treatment included *Xcr1*:*Xcl1* between DC_1 or DC_2 and NK/T cells, as well as *IFNγr2*:*IFNγ* and *Il12rb2*:*Il12b* between DC_3 or DC_1 and NK/T cells (Fig. 5C and D), among others (Supplementary Fig. S6C).

We next compared expression levels of ligands and receptors identified in this study in lung cancer-bearing mice to that in human DC states and NK/T cells (Supplementary Fig. S6D). The transcript abundances for these genes in each cell type were closely correlated between vehicle-treated KP1.9 lung cancer-bearing mice and human cells from untreated patients with NSCLC (Fig. 5E), showing that gene expression among these three DC states was conserved between species.

Although both DC_1 and DC_3 expressed *Il12b*, the strongest increase of gene expression was detected in DC_3 following CSF1Ri treatment (Fig. 5C, D, and F; Supplementary Fig. S6E). CSF1Ri-induced gene expression changes in each DC state are shown in Supplementary Fig. S6F–S6J. These findings indicate that *Il12b* was an enriched DC gene that emerged among the new DC-NK/T-cell interactions in response to CSF1Ri treatment, and this gene was primarily upregulated by the DC_3 state. On the basis of these data, we next used *Batf3*-deficient mice to interrogate the role of DCs in CSF1Ri-mediated antitumor immunity. In the absence of Batf3, KP1.9 lung tumor control was lost in CSF1Ri-treated mice (Fig. 5G), indicating that DCs were required for a successful response to CSF1Ri treatment. We also found that genetic ablation of IL12p40 resulted in the loss of response to CSF1Ri treatment (Fig. 5H). These data indicate that Batf3-dependent DCs and IL12-producing cells were required for a successful response to treatment. Of note, both DC_1 and DC_3 compartments are compromised in Batf3-deficient mice (22) and a small fraction of DC_1 produced *Il12b* in response to CSF1Ri treatment, leaving open the possibility that DC_1 also execute antitumor functions in the context of this treatment. A summary of the efficacy of CSF1Ri treatment in mice presenting different genotypes further illustrates the relevance of the cytokines IFNγ and IL12, and the transcription factor Batf3, in enabling tumor control (Supplementary Fig. S6K). We used relative lung weights to present summary data from independently performed experiments because tumor cells exhibited different *in vivo* growth kinetics in the KO and WT mouse strains analyzed. Together, lung weight measurements in WT, *IFNγ*$^{-/-}$, *Batf3*$^{-/-}$, and *Il12p40*$^{-/-}$ mice receiving CSF1Ri or vehicle-only treatment (Figs. 1B, 4H, 5G, and 5H; Supplementary Fig. S6K) suggest that CSF1Ri treatment induced new interactions between

NK cells, T cells, and DC_3, and that DC_3-produced IL12 mediated one of the interactions that was required for CSF1Ri-driven antitumor immunity.

Discussion

Given that only a small fraction of patients benefit from current immunotherapies, there is an interest to discover orthogonal mechanisms to trigger durable immune clearance of tumors. One apparent therapeutic opportunity is in targeting so-called “cold tumors,” in which T cells fail to penetrate tumors. In this context, macrophage-focused therapies may serve to recruit T cells and thus sensitize tumors, considering that macrophages often abound within tumors, including those that lack T cells.

Immunotherapies could mediate “cold tumor” clearance by at least two different types of mechanism: those that directly alleviate T-cell inhibition, and those that indirectly alleviate the immunosuppressive microenvironment maintained by tumor and innate immune cells. In T cell–focused treatments, studies in mice have suggested that a key mechanism for durable T-cell response is not merely autonomous to the T cells being targeted. Rather, the efficacy of immunotherapies targeting T cells may depend on a T cell–DC licensing loop (37, 66–69) and downstream IFNγ signaling (70). For instance, T cell–focused therapies may kick-start a positive feedback by stimulating antigen-presenting DCs via IFNγ produced by T cells, which in turn further activate T cells and license these cells’ effector functions through production of IL12 (37). Loss of either arms of this crucial signaling feedback loop leads to loss of tumor control (37). Conversely, immune drugs that target either IFNγ-producing T cells (e.g., antagonistic anti–PD-1) or IL12-producing DCs (e.g., agonistic anti-CD40) can be used to activate the T cell–DC licensing loop. Much less is known about the mechanisms that lead to tumor regression upon targeting other immune cells.

Here, we investigated the mechanism of action of an alternative immunotherapy that acts by inhibiting CSF1R. Drugs targeting CSF1R are not expected to act directly on T cells, as CSF1R is expressed specifically by phagocytes of the innate immune system, predominantly macrophages and their monocyte precursors. In addition, the drug we used for this study, BLZ945, was previously shown to have an affinity for CSF1R that is at least three orders of magnitude higher than its affinity for other kinases, and thus perturbs macrophages specifically through CSF1R targeting (21), although we cannot rule out off-target interactions through factors other than kinases. Our starting point was to show that CSF1R inhibition controls tumor growth in a mouse model of lung adenocarcinoma that is: (i) driven by common genetic alterations (mutated *Kras* and loss of *Trp53*), (ii) largely lacking T cells within the tumor mass, (iii) untreatable with currently approved treatments. This provided us with a working model in which to dissect CSF1R inhibition’s mechanism of action. Contrary to our expectations, we found evidence that CSF1R inhibition can act by a mechanism that converges on the same core T cell–DC licensing loop that mediates T-cell immunotherapies and also requires the cytokines IL12 and IFNγ. Intriguingly, CSF1R inhibition appeared to first initiate a response via NK cells, providing a possible explanation for how the response can be activated prior to successful tumor infiltration by T cells.

To gain insight into the action of CSF1R inhibition, we made use of scRNA-seq, which offers a holistic view of how the tumor immune cell repertoire changes following treatment, without making assumptions about the role of any particular cell type in the process. This analysis showed that CSF1R inhibition altered the activity of monocyte and macrophage subsets, but did not coherently affect classically defined “pro-” or “anti-” inflammatory effector functions in these cells. Instead, the major changes in $CSF1R^+$ cell states manifested in altered cytokine expression and upregulated stimulatory signals to T and NK cells as well as DCs. A unique subset of activated DCs, named here intratumoral DC_3 (10, 65), expressed increased levels of IL12, thus opening the possibility to initiate IL12/IFNγ feedback. Interestingly, meta-analysis of scRNA-seq studies revealed that DC_3 are conserved across patients, regardless of the tissue in which these cells reside, the genetic makeup of tumor cells, and the composition of the TME (65). Furthermore, unsupervised hierarchical clustering revealed that DC_3 are conserved between humans and mice (10), underscoring the value of murine tumor models to study these cells. Other names used to refer to the tumor-infiltrating DC_3 state include mregDC (64), $LAMP3^+$ DCs (71), and $CCR7^+$ DCs (72). Our data are in line with previous work done in a mammary carcinoma mouse model, which showed that an interference with the CSF1/CSF1R signaling pathway using a CSF1 blocking antibody also resulted in increased DC-mediated IL12 production at the tumor site and elicited T-cell responses that were relevant for tumor control in a chemotherapeutic setting (28). In line with the latter study, additional work testing CSF1/CSF1R blockade strategies (23–25) showed boosting of T-cell responses as being important for treatment efficacy.

In our study, we further show the relevance of NK-cell activation following CSF1R inhibition; this process may be especially relevant for tumors that lack T cells and are unresponsive to current T cell–centric immunotherapies. Loss of NK cells was sufficient to render CSF1R inhibition therapy ineffective in this model. NK cells may be required to kick-start the positive feedback loop because T cells were virtually excluded from KP1.9 tumors prior to treatment (34), but eventually penetrated the tumor tissue during an effective treatment response. In contrast, NK cells were detected within lung tumor nodules already in absence of CSF1Ri treatment, although in low numbers. This accords with previous findings that enhancers of antitumor DC responses include XCL1 (73) and Flt3 L (74), which can both be produced by NK cells. In fact, *Xcl1* and *Flt3L* expression was higher in KP1.9 tumor-infiltrating NK cells from CSF1Ri-treated mice when compared with vehicle-treated controls. Also, NK cells increased expression of the *Il12* receptor, likely further fostering the positive feedback loop between DCs and NK cells. Future work is needed to identify how macrophages affect the potency of this central antitumoral cytokine-driven cross-talk. Specific immunoregulatory molecules could play a role. For example, *C1qa* has known immunosuppressive functions when produced by macrophages (75), and we found that its expression in macrophages decreased following CSF1Ri treatment. It is also possible that discrete macrophage states are preferentially involved with suppressing the antitumoral cross-talk. Moreover, we show that monocytes/macrophages have a strong heterogeneity and that the abundance of substates changes following CSF1R blockade. For example, $Mø_1$ and $Mø_3$ exhibited tumor-promoting phenotypes and their prevalence decreased following drug treatment.

Neither IFNγ-secreting NK cells or T cells nor IL12-producing DCs expressed CSF1R at significant level, in line with the notion that the response of these cells was indirectly mediated via $CSF1R^+$ cells. Thus, in this model, macrophage targeting appears not to define an independent route to control tumors. Instead, the response converges to the same pathway relevant to activation of the adaptive immune response. Promisingly, the ligand–receptor pairs responding to CSF1Ri treatment correlate strongly in their expression across cell types between this mouse lung tumor model and human NSCLC patient samples.

In summary, targeting tumors by CSF1Ri treatment may not present an orthogonal or independent mechanistic route to control tumors as compared with existing T cell–focused immunotherapies. Instead, changes to CSF1R-expressing cells may trigger the same key events relevant to activation of the adaptive immune response, via a positive feedback loop between IL12 and IFNγ. We do not know whether this mechanism will turn out to be a hallmark of other myeloid-based immunotherapies. If so, the complexity of immune signaling might be better understood by establishing whether or not this single enabling feedback loop is triggered.

Supplementary Material

Refer to Web version on PubMed Central for supplementary material.

Acknowledgments

The authors thank the Harvard Stem Cell Institute for help with FACS sorting; the Single-Cell Core Facility at Harvard Medical School for inDrop reagents; the Bauer Core Facility for sequencing; members of the Hope Babette Tang Histology Facility at the Koch Institute Swanson Biotechnology Center and Yoshiko Iwamoto from the MGH Center for Systems Biology for technical support; and the Klein, Pittet, and Weissleder lab members for helpful discussions. This work was supported in part by the ISREC Foundation; the Samana Cay MGH Research Scholar Fund; the Robert Wenner Award from the Swiss Cancer League; and NIH grants R01-CA218579 (to A.M. Klein and M.J. Pittet), R01-AI084880 and R01-AI123349 (to M.J. Pittet), R01-CA206890 (to M.J. Pittet and R. Weissleder), and R33-CA202064 and U01CA206997 (to R. Weissleder). C. Pfirschke was supported in part by the MGH ECOR Tosteson Postdoctoral Fellowship; R. Zilionis was supported in part by the European Regional Development Fund (project number 01.2.2-LMT-K-718-04-0002) under grant agreement with the Research Council of Lithuania; A.E. Zou was supported by National Institute of General Medical Sciences T32 GM007753; S. Rickelt was supported by the MIT Ludwig Center for Molecular Oncology and funding from Richard O. Hynes (NIH grant U54-CA163109); and R. Bill was funded by a Postdoc.Mobility Fellowship of the Swiss National Science Foundation (SNSF; P400PM_183852).

References

1. Noy R, Pollard JW. Tumor-associated macrophages: from mechanisms to therapy. Immunity 2014;41:49–61. [PubMed: 25035953]
2. Engblom C, Pfirschke C, Pittet MJ. The role of myeloid cells in cancer therapies. Nat Rev Cancer 2016;16:447–62. [PubMed: 27339708]
3. DeNardo DG, Ruffell B. Macrophages as regulators of tumour immunity and immunotherapy. Nat Rev Immunol 2019;19:369–82. [PubMed: 30718830]
4. Zhang QW, Liu L, Gong CY, Shi HS, Zeng YH, Wang XZ, et al. Prognostic significance of tumor-associated macrophages in solid tumor: a meta-analysis of the literature. PLoS One 2012;7:e50946.
5. Steidl C, Lee T, Shah SP, Farinha P, Han G, Nayar T, et al. Tumor-associated macrophages and survival in classic Hodgkin's lymphoma. N Engl J Med 2010; 362:875–85. [PubMed: 20220182]
6. Ruffell B, Coussens LM. Macrophages and therapeutic resistance in cancer. Cancer Cell 2015;27:462–72. [PubMed: 25858805]

7. Sica A, Larghi P, Mancino A, Rubino L, Porta C, Totaro MG, et al. Macrophage polarization in tumour progression. Semin Cancer Biol 2008;18:349–55. [PubMed: 18467122]
8. Mills CD. M1 and M2 macrophages: oracles of health and disease. Crit Rev Immunol 2012;32:463–88. [PubMed: 23428224]
9. Sica A, Mantovani A. Macrophage plasticity and polarization: in vivo veritas. J Clin Invest 2012;122:787–95. [PubMed: 22378047]
10. Zilionis R, Engblom C, Pfirschke C, Savova V, Zemmour D, Saatcioglu HD, et al. Single-cell transcriptomics of human and mouse lung cancers reveals conserved myeloid populations across individuals and species. Immunity 2019;50:1317–34. [PubMed: 30979687]
11. Cassetta L, Fragkogianni S, Sims AH, Swierczak A, Forrester LM, Zhang H, et al. Human tumor-associated macrophage and monocyte transcriptional landscapes reveal cancer-specific reprogramming, biomarkers, and therapeutic targets. Cancer Cell 2019;35:588–602. [PubMed: 30930117]
12. Ginhoux F, Schultze JL, Murray PJ, Ochando J, Biswas SK. New insights into the multidimensional concept of macrophage ontogeny, activation and function. Nat Immunol 2016;17:34–40. [PubMed: 26681460]
13. Mantovani A, Marchesi F, Malesci A, Laghi L, Allavena P. Tumour-associated macrophages as treatment targets in oncology. Nat Rev Clin Oncol 2017;14: 399–416. [PubMed: 28117416]
14. Gubin MM, Esaulova E, Ward JP, Malkova ON, Runci D, Wong P, et al. High-dimensional analysis delineates myeloid and lymphoid compartment remodeling during successful immune-checkpoint cancer therapy. Cell 2018; 175:1014–30. [PubMed: 30343900]
15. Kowal J, Kornete M, Joyce JA. Re-education of macrophages as a therapeutic strategy in cancer. Immunotherapy 2019;11:677–89. [PubMed: 31088236]
16. Cassetta L, Pollard JW. Targeting macrophages: therapeutic approaches in cancer. Nat Rev Drug Discov 2018;17:887–904. [PubMed: 30361552]
17. Chiu JW, Hotte SJ, Kollmannsberger CK, Renouf DJ, Cescon DW, Hedley D, et al. A phase I trial of ANG1/2-Tie2 inhibitor trebaninib (AMG386) and temsirolimus in advanced solid tumors (PJC008/NCI]9041). Invest New Drugs 2016;34:104–11. [PubMed: 26686201]
18. Lei F, Cui N, Zhou C, Chodosh J, Vavvas DG, Paschalis EI. CSF1R inhibition by a small-molecule inhibitor is not microglia specific; affecting hematopoiesis and the function of macrophages. Proc Natl Acad Sci U S A 2020;117:23336–8. [PubMed: 32900927]
19. Ries CH, Cannarile MA, Hoves S, Benz J, Wartha K, Runza V, et al. Targeting tumor-associated macrophages with anti-CSF-1R antibody reveals a strategy for cancer therapy. Cancer Cell 2014;25:846–59. [PubMed: 24898549]
20. Yan D, Kowal J, Akkari L, Schuhmacher AJ, Huse JT, West BL, et al. Inhibition of colony stimulating factor-1 receptor abrogates microenvironment-mediated therapeutic resistance in gliomas. Oncogene 2017;36:6049–58. [PubMed: 28759044]
21. Pyonteck SM, Akkari L, Schuhmacher AJ, Bowman RL, Sevenich L, Quail DF, et al. CSF-1R inhibition alters macrophage polarization and blocks glioma progression. Nat Med 2013;19:1264–72. [PubMed: 24056773]
22. Zhang L, Li Z, Skrzypczynska KM, Fang Q, Zhang W, O'Brien SA, et al. Single-cell analyses inform mechanisms of myeloid-targeted therapies in colon cancer. Cell 2020;181:442–59. [PubMed: 32302573]
23. Zhu Y, Knolhoff BL, Meyer MA, Nywening TM, West BL, Luo J, et al. CSF1/ CSF1R blockade reprograms tumor-infiltrating macrophages and improves response to T-cell checkpoint immunotherapy in pancreatic cancer models. Cancer Res 2014;74:5057–69. [PubMed: 25082815]
24. Hoves S, Ooi CH, Wolter C, Sade H, Bissinger S, Schmittnaegel M, et al. Rapid activation of tumor-associated macrophages boosts preexisting tumor immunity. J Exp Med 2018;215:859–76. [PubMed: 29436396]
25. Perry CJ, Munõz-Rojas AR, Meeth KM, Kellman LN, Amezquita RA, Thakral D, et al. Myeloid-targeted immunotherapies act in synergy to induce inflammation and antitumor immunity. J Exp Med 2018;215:877–93. [PubMed: 29436395]

26. Xu J, Escamilla J, Mok S, David J, Priceman S, West B, et al. CSF1R signaling blockade stanches tumor-infiltrating myeloid cells and improves the efficacy of radiotherapy in prostate cancer. Cancer Res 2013;73:2782–94. [PubMed: 23418320]
27. Akkari L, Bowman RL, Tessier J, Klemm F, Handgraaf SM, de Groot M, et al. Dynamic changes in glioma macrophage populations after radiotherapy reveal CSF-1R inhibition as a strategy to overcome resistance. Sci Transl Med 2020;12: eaaw7843.
28. Ruffell B, Chang-Strachan D, Chan V, Rosenbusch A, Ho CM, Pryer N, et al. Macrophage IL-10 blocks CD8+ T cell-dependent responses to chemotherapy by suppressing IL-12 expression in intratumoral dendritic cells. Cancer Cell 2014;26:623–37. [PubMed: 25446896]
29. Cassier PA, Italiano A, Gomez-Roca CA, Le Tourneau C, Toulmonde M, Cannarile MA, et al. CSF1R inhibition with emactuzumab in locally advanced diffuse-type tenosynovial giant cell tumours of the soft tissue: a dose-escalation and dose-expansion phase 1 study. Lancet Oncol 2015;16:949–56. [PubMed: 26179200]
30. Bray F, Ferlay J, Soerjomataram I, Siegel RL, Torre LA, Jemal A. Global cancer statistics 2018: GLOBOCAN estimates of incidence and mortality worldwide for 36 cancers in 185 countries. CA Cancer J Clin 2018;68:394–424. [PubMed: 30207593]
31. Siegel RL, Miller KD, Jemal A. Cancer statistics, 2020. CA Cancer J Clin 2020;70: 7–30. [PubMed: 31912902]
32. Zhang BC, Gao J, Wang J, Rao ZG, Wang BC, Gao JF. Tumor-associated macrophages infiltration is associated with peritumoral lymphangiogenesis and poor prognosis in lung adenocarcinoma. Med Oncol 2011;28:1447–52. [PubMed: 20676804]
33. Lavin Y, Kobayashi S, Leader A, Amir ED, Elefant N, Bigenwald C, et al. Innate immune landscape in early lung adenocarcinoma by paired single-cell analyses. Cell 2017;169:750–65. [PubMed: 28475900]
34. Pfirschke C, Engblom C, Rickelt S, Cortez-Retamozo V, Garris C, Pucci F, et al. Immunogenic chemotherapy sensitizes tumors to checkpoint blockade therapy. Immunity 2016;44:343–54. [PubMed: 26872698]
35. DuPage M, Dooley AL, Jacks T. Conditional mouse lung cancer models using adenoviral or lentiviral delivery of Cre recombinase. Nat Protoc 2009;4:1064–72. [PubMed: 19561589]
36. Cuccarese MF, Dubach JM, Pfirschke C, Engblom C, Garris C, Miller MA, et al. Heterogeneity of macrophage infiltration and therapeutic response in lung carcinoma revealed by 3D organ imaging. Nat Commun 2017;8:14293. [PubMed: 28176769]
37. Garris CS, Arlauckas SP, Kohler RH, Trefny MP, Garren S, Piot C, et al. Successful anti-PD-1 cancer immunotherapy requires T cell-dendritic cell cross-talk involving the cytokines IFN-g and IL-12. Immunity 2018;49:1148–61. [PubMed: 30552023]
38. Zilionis R, Nainys J, Veres A, Savova V, Zemmour D, Klein AM, et al. Single-cell barcoding and sequencing using droplet microfluidics. Nat Protoc 2017;12:44–73. [PubMed: 27929523]
39. Klein AM, Mazutis L, Akartuna I, Tallapragada N, Veres A, Li V, et al. Droplet barcoding for single-cell transcriptomics applied to embryonic stem cells. Cell 2015;161:1187–201. [PubMed: 26000487]
40. Weinreb C, Wolock S, Klein AM. SPRING: a kinetic interface for visualizing high dimensional single-cell expression data. Bioinformatics 2018;34:1246–8. [PubMed: 29228172]
41. Wolock SL, Lopez R, Klein AM. Scrublet: computational identification of cell doublets in single-cell transcriptomic data. Cell Syst 2019;8:281–91. [PubMed: 30954476]
42. Zemmour D, Zilionis R, Kiner E, Klein AM, Mathis D, Benoist C. Single-cell gene expression reveals a landscape of regulatory T cell phenotypes shaped by the TCR. Nat Immunol 2018;19:291–301. [PubMed: 29434354]
43. Jaitin DA, Kenigsberg E, Keren-Shaul H, Elefant N, Paul F, Zaretsky I, et al. Massively parallel single-cell RNA-seq for marker-free decomposition of tissues into cell types. Science 2014;343:776–9. [PubMed: 24531970]
44. Korotkevich G, Sukhov V, Sergushichev A. Fast gene set enrichment analysis. BioRxiv 060012 [Preprint]. 2019. Available from: 10.1101/060012.

45. Ashburner M, Ball CA, Blake JA, Botstein D, Butler H, Cherry JM, et al. Gene ontology: tool for the unification of biology. The Gene Ontology Consortium. Nat Genet 2000;25:25–9. [PubMed: 10802651]
46. Subramanian A, Tamayo P, Mootha VK, Mukherjee S, Ebert BL, Gillette MA, et al. Gene set enrichment analysis: a knowledge-based approach for interpreting genome-wide expression profiles. Proc Natl Acad Sci U S A 2005;102:15545–50. [PubMed: 16199517]
47. Ramilowski JA, Goldberg T, Harshbarger J, Kloppmann E, Kloppman E, Lizio M, et al. A draft network of ligand-receptor-mediated multicellular signalling in human. Nat Commun 2015;6:7866. [PubMed: 26198319]
48. Breuer K, Foroushani AK, Laird MR, Chen C, Sribnaia A, Lo R, et al. InnateDB: systems biology of innate immunity and beyond–recent updates and continuing curation. Nucleic Acids Res 2013;41:D1228–33. [PubMed: 23180781]
49. Efremova M, Vento-Tormo M, Teichmann SA, Vento-Tormo R. CellPhoneDB: inferring cell-cell communication from combined expression of multi-subunit ligand-receptor complexes. Nat Protoc 2020;15:1484–506. [PubMed: 32103204]
50. Cortez-Retamozo V, Etzrodt M, Newton A, Rauch PJ, Chudnovskiy A, Berger C, et al. Origins of tumor-associated macrophages and neutrophils. Proc Natl Acad Sci U S A 2012;109:2491–6. [PubMed: 22308361]
51. Lawrence T, Natoli G. Transcriptional regulation of macrophage polarization: enabling diversity with identity. Nat Rev Immunol 2011;11:750–61. [PubMed: 22025054]
52. Etzerodt A, Tsalkitzi K, Maniecki M, Damsky W, Delfini M, Baudoin E, et al. Specific targeting of CD163^{+} TAMs mobilizes inflammatory monocytes and promotes T cell-mediated tumor regression. J Exp Med 2019;216:2394–411. [PubMed: 31375534]
53. Arlauckas SP, Garren SB, Garris CS, Kohler RH, Oh J, Pittet MJ, et al. Arg1 expression defines immunosuppressive subsets of tumor-associated macrophages. Theranostics 2018;8:5842–54. [PubMed: 30613266]
54. Herber DL, Cao W, Nefedova Y, Novitskiy SV, Nagaraj S, Tyurin VA, et al. Lipid accumulation and dendritic cell dysfunction in cancer. Nat Med 2010;16:880–6. [PubMed: 20622859]
55. Galon J, Angell HK, Bedognetti D, Marincola FM. The continuum of cancer immunosurveillance: prognostic, predictive, and mechanistic signatures. Immunity 2013;39:11–26. [PubMed: 23890060]
56. Zaretsky JM, Garcia-Diaz A, Shin DS, Escuin-Ordinas H, Hugo W, Hu-Lieskovan S, et al. Mutations associated with acquired resistance to PD-1 blockade in melanoma. N Engl J Med 2016;375:819–29. [PubMed: 27433843]
57. Best JA, Blair DA, Knell J, Yang E, Mayya V, Doedens A, et al. Transcriptional insights into the CD8(+) T cell response to infection and memory T cell formation. Nat Immunol 2013;14:404–12. [PubMed: 23396170]
58. Utzschneider DT, Charmoy M, Chennupati V, Pousse L, Ferreira DP, Calderon-Copete S, et al. T cell factor 1-expressing memory-like CD8(+) T cells sustain the immune response to chronic viral infections. Immunity 2016;45:415–27. [PubMed: 27533016]
59. Szabo SJ, Kim ST, Costa GL, Zhang X, Fathman CG, Glimcher LH. A novel transcription factor, T-bet, directs Th1 lineage commitment. Cell 2000;100: 655–69. [PubMed: 10761931]
60. Liu CC, Walsh CM, Young JD. Perforin: structure and function. Immunol Today 1995;16:194–201. [PubMed: 7734048]
61. Flesch IE, Hess JH, Huang S, Aguet M, Rothe J, Bluethmann H, et al. Early interleukin 12 production by macrophages in response to mycobacterial infection depends on interferon gamma and tumor necrosis factor alpha. J Exp Med 1995;181:1615–21. [PubMed: 7722441]
62. Weissleder R, Nahrendorf M, Pittet MJ. Imaging macrophages with nanoparticles. Nat Mater 2014;13:125–38. [PubMed: 24452356]
63. Di Pilato M, Kfuri-Rubens R, Pruessmann JN, Ozga AJ, Messemaker M, Cadilha BL, et al. CXCR6 positions cytotoxic T cells to receive critical survival signals in the tumor microenvironment. Cell 2021;184:4512–30. [PubMed: 34343496]
64. Maier B, Leader AM, Chen ST, Tung N, Chang C, LeBerichel J, et al. A conserved dendritic-cell regulatory program limits antitumour immunity. Nature 2020; 580:257–62. [PubMed: 32269339]

65. Gerhard GM, Bill R, Messemaker M, Klein AM, Pittet MJ. Tumor-infiltrating dendritic cell states are conserved across solid human cancers. J Exp Med 2021; 218:e20200264.

66. Schlitzer A, Ginhoux F. Organization of the mouse and human DC network. Curr Opin Immunol 2014;26:90–9. [PubMed: 24556405]

67. Hildner K, Edelson BT, Purtha WE, Diamond M, Matsushita H, Kohyama M, et al. Batf3 deficiency reveals a critical role for CD8alpha+ dendritic cells in cytotoxic T cell immunity. Science 2008;322:1097–100. [PubMed: 19008445]

68. MartIn-Fontecha A, Sebastiani S, Ho€pken UE, Uguccioni M, Lipp M, Lanzavecchia A, et al. Regulation of dendritic cell migration to the draining lymph node: impact on T lymphocyte traffic and priming. J Exp Med 2003; 198:615–21. [PubMed: 12925677]

69. de Mingo Pulido Á, Gardner A, Hiebler S, Soliman H, Rugo HS, Krummel MF, et al. TIM-3 regulates $CD103^{+}$ dendritic cell function and response to chemotherapy in breast cancer. Cancer Cell 2018;33:60–74. [PubMed: 29316433]

70. Grasso CS, Tsoi J, Onyshchenko M, Abril-Rodriguez G, Ross-Macdonald P, Wind-Rotolo M, et al. Conserved interferon-g signaling drives clinical response to immune checkpoint blockade therapy in melanoma. Cancer Cell 2020;38:500–15. [PubMed: 32916126]

71. Zhang Q, He Y, Luo N, Patel SJ, Han Y, Gao R, et al. Landscape and dynamics of single immune cells in hepatocellular carcinoma. Cell 2019;179:829–45. [PubMed: 31675496]

72. Qian J, Olbrecht S, Boeckx B, Vos H, Laoui D, Etlioglu E, et al. A pan-cancer blueprint of the heterogeneous tumor microenvironment revealed by single-cell profiling. Cell Res 2020;30:745–62. [PubMed: 32561858]

73. Boöttcher JP, Bonavita E, Chakravarty P, Blees H, Cabeza-Cabrerizo M, Sammicheli S, et al. NK cells stimulate recruitment of cDC1 into the tumor microenvironment promoting cancer immune control. Cell 2018;172: 1022–37. [PubMed: 29429633]

74. Barry KC, Hsu J, Broz ML, Cueto FJ, Binnewies M, Combes AJ, et al. A natural killer-dendritic cell axis defines checkpoint therapy-responsive tumor microenvironments. Nat Med 2018;24:1178–91. [PubMed: 29942093]

75. Roumenina LT, Daugan MV, Noé R, Petitprez F, Vano YA, Sanchez-Salas R, et al. Tumor cells hijack macrophage-produced complement C1q to promote tumor growth. Cancer Immunol Res 2019;7:1091–105. [PubMed: 31164356]

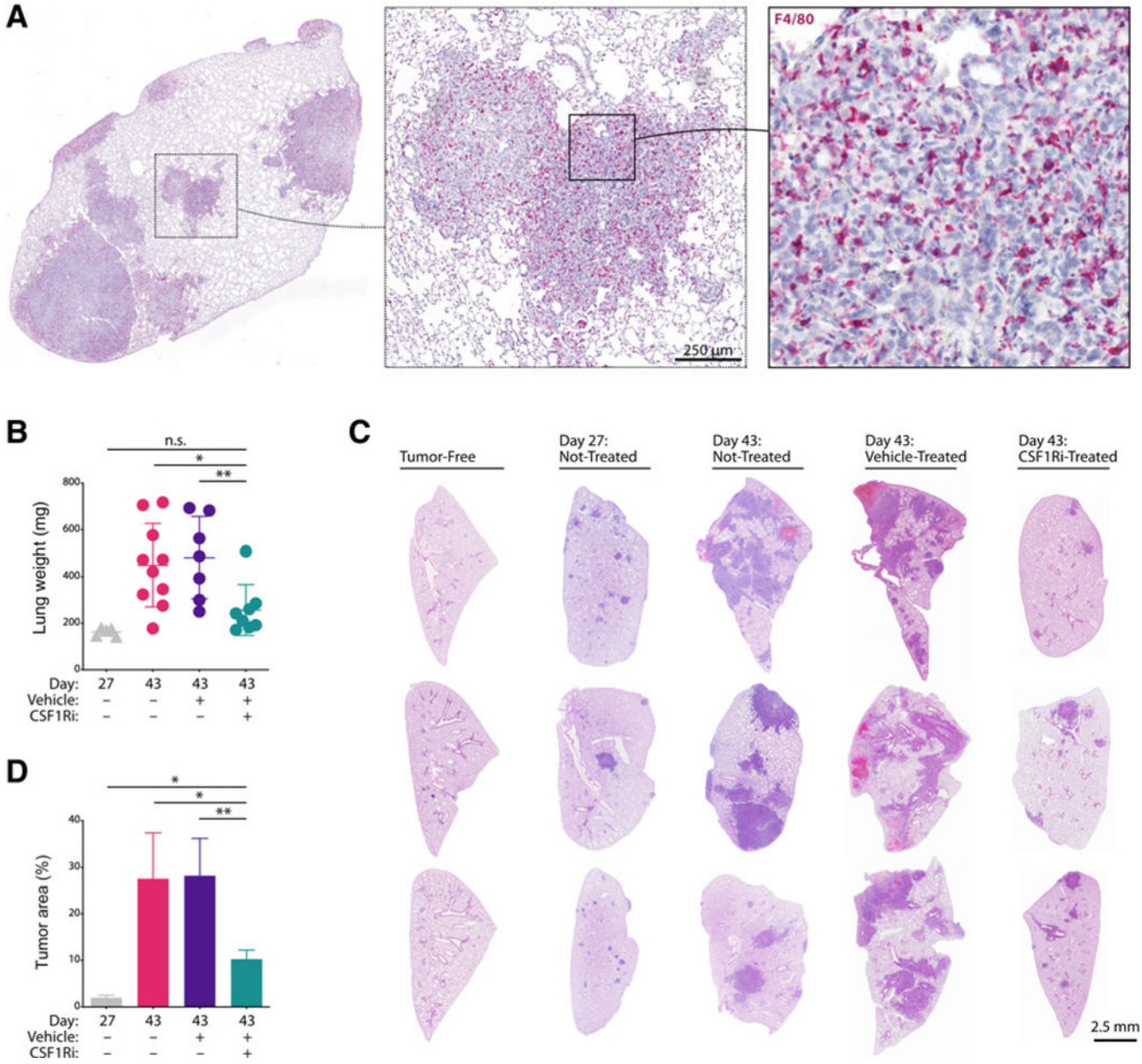

Figure 1.

CSF1Ri treatment controls KP1.9 lung adenocarcinoma progression. **A**, Representative F4/80 staining on a section from a formaldehyde-fixed and paraffin-embedded KP1.9 tumor–bearing lung of a C57BL/6J WT mouse euthanized on day 42 after intravenous tumor cell injection. Scale bar, 250 µm. **B,** Lung weight as proxy of tumor burden in KP1.9 tumor–bearing mice (C57BL/6J WT mice) following 2 weeks of treatment with CSF1Ri or vehicle (day 43 after intravenous tumor cell injection). Drug treatment started on day 29. Tumor-bearing lungs of untreated mice were analyzed as controls at before and after treatment time points (day 27 and day 43). n = 5–10 mice/group. Data are represented as mean ± SD. **C,** Representative images of H&E-stained lung lobe sections of KP1.9 tumor–bearing mice (C57BL/6J WT mice) treated or not with CSF1Ri or vehicle are shown at

prior and after treatment time points (day 27, day 43). Lung sections of tumor-free mice are presented in parallel. Scale bar, 2.5 mm. **D,** H&E-based quantification of percent tumor area per lung lobe section of C57BL/6J WT mice treated or not with CSF1Ri or vehicle (n = 3–12 mice/group), analyzed at before and after treatment time points (day 27 or day 43 after intravenous tumor cell injection). Data are represented as mean ± SEM. For comparisons between two groups, Student two-tailed t test was used. *, $P < 0.05$; **, $P < 0.01$. See also Supplementary Fig. S1.

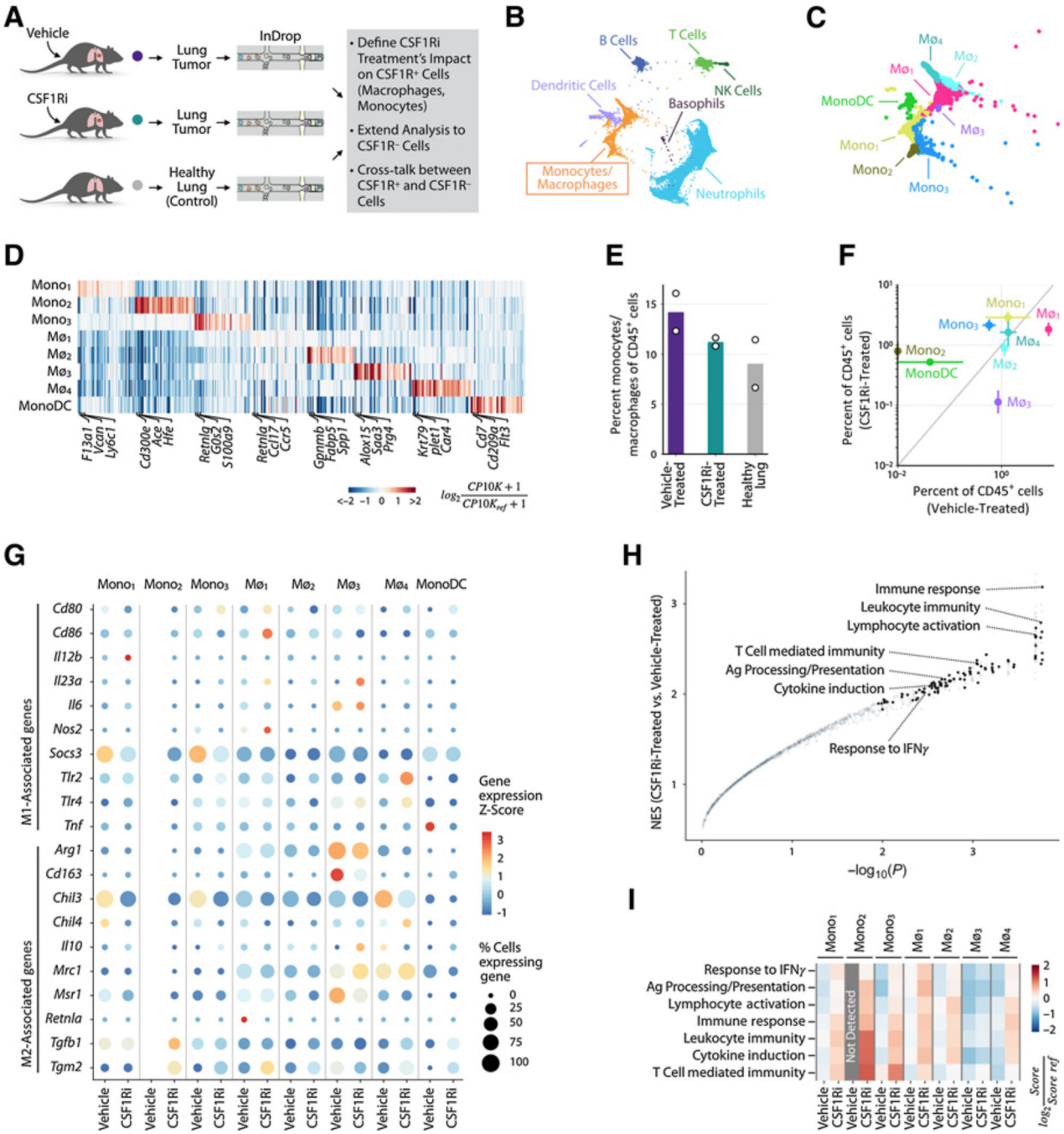

Figure 2.

CSF1Ri treatment reshapes the CSF1R$^+$ cell landscape in NSCLC. **A,** Schematic of experimental workflow for defining and comparing immune transcriptional states in lung tissue of KP1.9 tumor–bearing C57BL/6J WT mice treated or not with the CSF1Ri BLZ945 (CSF1Ri: $n = 2$; vehicle: $n = 2$) or of healthy tumor-free mice ($n = 2$). Single-cell suspensions were obtained from KP1.9 lung tumors of mice that were treated for 15 days with BLZ945 or vehicle control solution. Treatment started on day 29 following intravenous KP1.9 tumor cell injection, and lungs were harvested on day 44 for scRNA-

seq investigation. **B,** SPRING visualization of scRNA-seq data of lung immune cells combining all three conditions (9,854 cells lung tumor CSF1Ri; 8,852 cells lung tumor vehicle; 6,333 cells healthy lung). Major cell types were annotated using a Bayesian cell classifier. **C,** SPRING plots of lung monocyte/macrophage states from mouse KP1.9 lung tumor and healthy lung tissues. Zoomed-in view of the monocyte/macrophage cluster shown in orange in **B.** All conditions (vehicle-treated, CSF1Ri-treated, healthy lung) combined. **D,** Expression of genes expected (10) to be enriched within monocyte/ macrophage states. CP10K, counts per ten thousand. $CP10K_{ref}$, second-highest expression value among monocyte/ macrophage states. **E,** Relative abundance of monocyte/macrophage states from scRNA-seq data in KP1.9 tumor–bearing (vehicle-treated, CSF1Ri-treated) or tumor-free lungs. Dots represent biological replicates. **F,** The CSF1Ri enrichment of monocyte/macrophage states assessed by plotting their frequency in CSF1Ri-treated versus vehicle-treated samples. Bars show the two-replicate value of each condition. **G,** Expression of M1- and M2-associated gene panels in monocyte and macrophage states from vehicle- and CSF1Ri-treated KP1.9 lung tumors. Circle color shows relative average expression within monocyte/macrophage states; circle size shows percentage of cells within state expressing gene. The monocyte substate $Mono_2$ was not detected in vehicle-treated tumor-bearing lungs. **H,** GO terms with normalized enrichment score (NES) > 0 in monocytes/ macrophages following CSF1Ri treatment as compared with vehicle treatment, plotted against *P* value. Black circles denote immune-related GO terms that are significantly enriched with CSF1Ri ($P_{adjusted} < 0.05$); gray circles denote non-enriched processes. I, Relative pathway scores for GO terms labeled in **H** among monocyte and macrophage states in vehicle- and CSF1Ri-treated KP1.9 lung tumors. $Score_{REF}$, median pathway score. See also Supplementary Figs. S2 and S3.

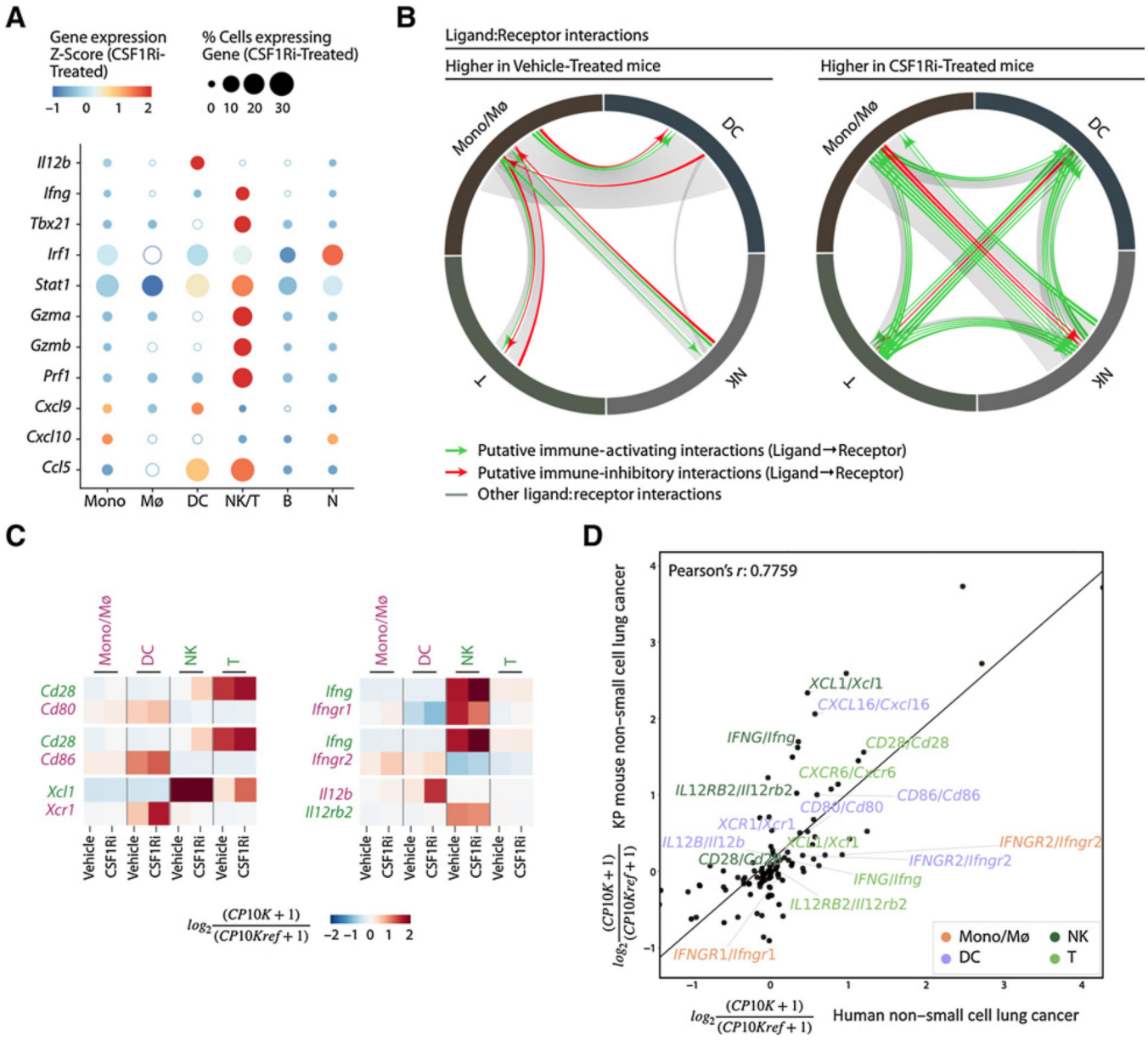

Figure 3.

CSF1Ri rewires cellular cross-talk in the TME. **A,** Expression of cytotoxicity-associated gene panel in immune populations [monocytes (Mono), macrophages (Mø), DCs, NK/T cells (NK/T), B cells (B), neutrophils (N)] from CSF1Ri-treated KP1.9 lung tumors. Circle color shows relative expression in CSF1Ri-treated tumors; circle size shows percentage of cells expressing gene. Circle is filled if gene expression increased with CSF1Ri compared with vehicle treatment and unfilled if expression was unchanged or decreased. **B,** Putative ligand–receptor interactions between DCs, monocytes/macrophages (Mono/Mø), NK cells (NK), and T cells (T) predicted to be altered with CSF1Ri treatment. Arrows drawn from ligand-expressing population to receptor-expressing population. Interactions colored based on annotated function or shaded gray if unannotated. **C,** Relative gene expression for selected ligands and receptors with putative immune-modulating interactions between

myeloid and lymphoid cell states, in vehicle- and CSF1Ri-treated mice with KP1.9 lung tumors. Interactions between $CSF1R^+$ monocytes/macrophages (Mono/Mø) or $CSF1R^-$ DCs highlighted in pink and $CSF1R^-$ T cells (T) or NK cells (NK) highlighted in green. $CP10K_{ref}$, median expression value per gene. The complete list of murine ligand–receptor interactions is presented in Supplementary Fig. S4C. **D,** Relative gene expression in tumors of untreated human patients with NSCLC (10) and vehicle-treated KP1.9 lung tumor–bearing mice for ligands and receptors shown in Supplementary Fig. S4C and S4D that are expressed on monocytes/macrophages (Mono/Mø), DCs, T cells (T), and NK cells (NK). Selected genes are highlighted for each cell type. See also Supplementary Fig. S4.

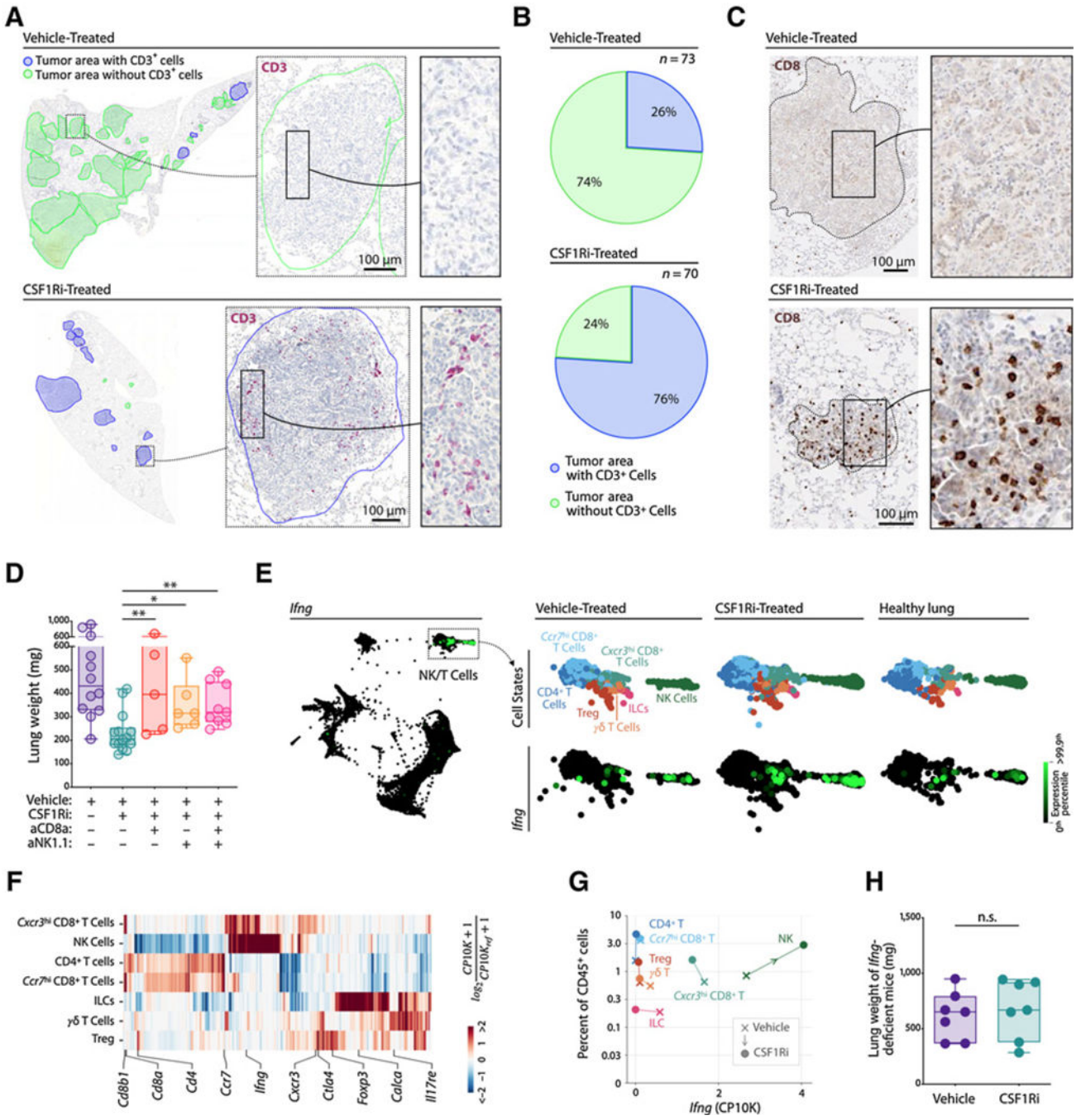

Figure 4.

CSF1Ri-driven antitumor immunity requires NK and T cells. **A,** Examples of KP1.9 lung tumor area quantification on CD3 and hematoxylin-stained lung lobe sections of vehicle- (top) or CSF1Ri-treated C57BL/6J WT mice (bottom). Consecutive H&E-stained sections were used to identify the tumor area on the CD3 stained sections. Mice were euthanized on day 43 following 2 weeks of treatment. Encircled tumor areas positive for CD3 (marked in blue) as well as tumor areas that lack CD3 staining (marked in green) are presented. Scale bars, 100 µm. **B,** Percent of tumor areas as indicated in **A** that contain $CD3^+$ cells

(blue) or lack CD3 staining (green) of 4–6 mice/group. Total number of analyzed tumor areas per condition is indicated (vehicle-treated, $n = 73$; CSF1Ri-treated, $n = 70$). **C,** Representative CD8 staining on KP1.9 lung tumor sections of vehicle- (top) or CSF1Ri-treated C57BL/6J WT mice (bottom). Treatment was conducted for 14 days, starting on day 29 after intravenous tumor cell injection, and mice were euthanized on day 43. Tumor areas are highlighted by black lines. Scale bars, 100 μm. **D,** Lung weight of CSF1Ri- or vehicle-treated KP1.9 lung tumor–bearing mice (C57BL/6J WT mice) that received CD8a (aCD8a)- or NK1.1 (aNK1.1)-depleting antibodies ($n = 5$–14 mice/group). The detailed treatment schedule is presented in Supplementary Fig. S5D. Data are represented as a box and whisker plot that shows quartiles and all data points from minimum to maximum. **E,** Single-cell expression of the gene *IFNγ* on the major cell type (left) and NK/T-cell state level (right; Tregs, ILCs, gd T cells, NK cells, $CD4^+$ T cells, $Ccr7^{hi}$ $CD8^+$ T cells, $Cxcr3^{hi}$ $CD8^+$ T cells) with separate treatment conditions in KP1.9 tumor and healthy lung samples via SPRING visualization. **F,** Enriched genes within NK/T cell states. $CP10K_{ref}$, median expression value among NK/T cell states. **G,** Change in mean *IFNg* expression and relative abundance of NK/T cell states between Vehicle-Treated and CSF1Ri-Treated samples. **H,** Lung weight of KP1.9 lung tumor–bearing IFNγ KO mice treated with CSF1Ri or vehicle for 10 days ($n = 7$ mice/group). Treatments started on day 25 after intravenous tumor cell injection, and mice were euthanized on day 35. Data are represented as a box and whisker plot that shows quartiles and all data points from minimum to maximum. For comparisons between two groups, Student two-tailed *t* test was used. *, $P < 0.05$; **, $P < 0.01$. See also Supplementary Fig. S5.

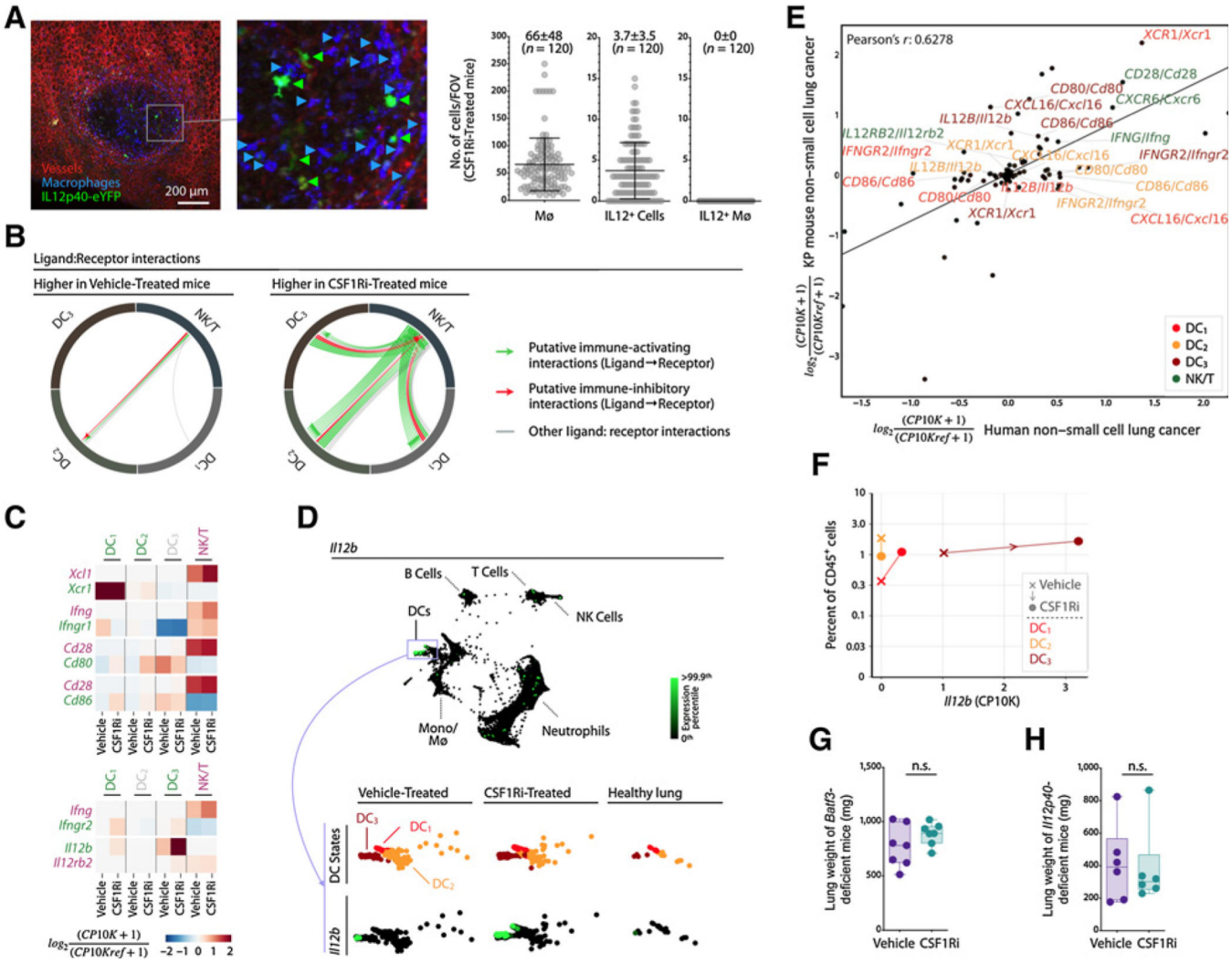

Figure 5.

CSF1Ri-driven antitumor immunity requires IL12 produced by dendritic cells. **A,** Representative intravital microscopy images (left) and quantification (right) of explanted lung tissues from KP1.9 lung tumor–bearing IL12p40-IRES-eYFP reporter mice treated with CSF1Ri for 14 days ($n = 4$ mice). Treatments started on day 29 after intravenous tumor cell injection, and mice were euthanized on day 43. Explanted lungs were imaged for phagocytic cells including macrophages (blue arrowheads), vessels (red), and endogenous IL12-eYFP signal (green arrowheads). Macrophages and IL12-positive cells were manually quantified per field of view (FOV, $n = 120$). Tumor area is highlighted with a dotted red line. Scale bar, 200 mm. Data are represented as mean ± SD. **B,** Putative ligand–receptor interactions between dendritic cell subsets (DC_1, DC_2, DC_3) and NK/T cells (NK/T) predicted to be altered with CSF1Ri or vehicle treatment. Arrows drawn from ligand-expressing population to receptor-expressing population. Interactions colored on the basis of annotated function or shaded gray if unannotated. **C,** Relative gene expression for selected ligands and receptors with putative immune-modulating interactions between DC states (DC_1, DC_2, DC_3) shown in green and NK/T cells (NK/T) shown in pink, in vehicle-

and CSF1Ri-treated KP1.9 lung tumors. *CP10K*$_{ref}$, median expression value per gene. **D,** Single-cell expression of the gene *Il12b* on the major cell type (top) and DC state level (bottom) with separate treatment conditions in KP1.9 tumor and healthy lung samples via SPRING visualization. **E,** Relative gene expression in tumors of untreated human patients with NSCLC (10) and vehicle-treated murine KP1.9 lung tumors for ligands and receptors shown in Supplementary Fig. S6C and S6D that are expressed on DC states and NK/T cells. Selected genes are highlighted for each cell type. **F,** Change in mean *Il12b* expression and relative abundance of DC states between vehicle-treated and CSF1Ri-treated samples. **G,** Lung weight as proxy for tumor burden in KP1.9 lung tumor–bearing Batf3 KO mice treated with CSF1Ri or vehicle for 10 days (n 7 mice/group). Treatments started on day 25 after intravenous tumor cell injection, and mice were euthanized on day 35. Data are represented as a box and whisker plot that shows quartiles and all data points from minimum to maximum**. H,** Lung weight of CSF1Ri- or vehicle-treated KP1.9 lung tumor–bearing IL12p40 KO mice (n 6 mice/group). Mice were treated for 14 days. Treatment started on day 25 after intravenous tumor cell injection, and mice were euthanized on day 39. Data are represented as a box and whisker plot that shows quartiles and all data points from minimum to maximum. For comparisons between two groups, Student two-tailed t test was used. **, $P < 0.01$. See also Supplementary Fig. S6.